

Modeling Cell Populations Measured By Flow Cytometry With Covariates Using Sparse Mixture of Regressions

Sangwon Hyun^{*1}, Mattias Rolf Cape^{†2}, Francois Ribalet^{‡2}, and Jacob Bien^{§1}

¹*Department of Data Sciences and Operations, University of Southern California*

²*School of Oceanography, University of Washington*

August 5, 2022

Abstract

The ocean is filled with microscopic microalgae called phytoplankton, which together are responsible for as much photosynthesis as all plants on land combined. Our ability to predict their response to the warming ocean relies on understanding how the dynamics of phytoplankton populations is influenced by changes in environmental conditions. One powerful technique to study the dynamics of phytoplankton is flow cytometry, which measures the optical properties of thousands of individual cells per second. Today, oceanographers are able to collect flow cytometry data in real-time onboard a moving ship, providing them with fine-scale resolution of the distribution of phytoplankton across thousands of kilometers. One of the current challenges is to understand how these small and large scale variations relate to environmental conditions, such as nutrient availability, temperature, light and ocean currents. In this paper, we propose a novel sparse mixture of multivariate regressions model to estimate the time-varying phytoplankton subpopulations while simultaneously identifying the specific environmental covariates that are predictive of the observed changes to these subpopulations. We demonstrate the usefulness and interpretability of the approach using both synthetic data and real observations collected on an oceanographic cruise conducted in the north-east Pacific in the spring of 2017.

Keywords: *Mixture of regressions, Expectation-maximization, Flow cytometry, Sparse regression, Ocean, Microbiome, Phytoplankton, Clustering, Gating, Alternating direction method of multipliers*

1 Introduction

Marine phytoplankton are responsible for as much photosynthesis as all plants on land combined, making them a crucial part of the earth’s biogeochemical cycle and climate [Field et al., 1998]. A better understanding of the ecology of marine phytoplankton species and their relationship with the ocean environment is therefore important both to basic biology and to shedding light on their role in carbon dioxide uptake. In order to study these single cell organisms in the ocean, flow cytometry has been instrumental for the past three decades [Sosik et al., 2010].

Flow cytometry measures light scatter and fluorescence emission of individual cells at rates of up to thousands of cells per second. Light scattering is proportional to cell size, and fluorescence is unique to the emission spectra of pigments; these parameters can be used to identify populations

*sangwonh@usc.edu

†mcape@uw.edu

‡ribalet@uw.edu

§jbien@usc.edu

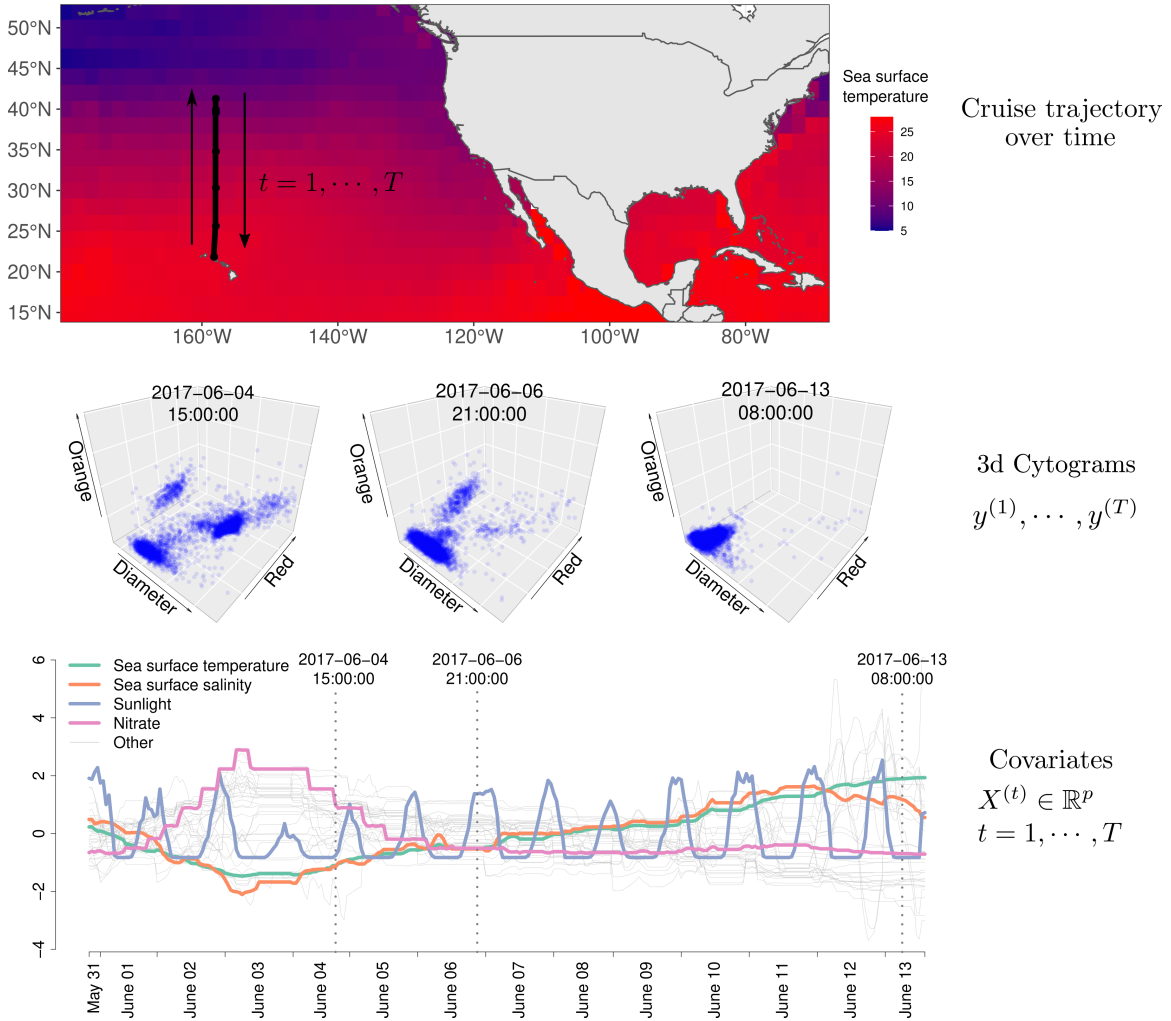


Figure 1: A schematic showing the data setup. (Top) This figure shows the trajectory of the Gradients 2 cruise, which moves North and then South along a trajectory starting at Hawaii. (Middle) The individual 3-dimensional particles are measured rapidly and continuously. From this, we form T cytograms $\mathbf{y}^{(t)}, t = 1, \dots, T$ at an hourly time resolution. The three data dimensions have simplified labels Red, Orange, and Diameter; the first two represent fluorescence emission, and the last measures cell diameter. (Bottom panel) At each time $t = 1, \dots, T$, environmental covariates $\mathbf{X}^{(t)} \in \mathbb{R}^p$ are also available through remote sensing and on-board measurements. Only a few of the 30+ normalized covariates are highlighted here. Our proposed model identifies subpopulations by modeling them as Gaussian clusters whose means and probabilities are driven by environmental covariates.

of phytoplankton with similar optical properties. Over the two decades, automated environmental flow cytometers such as CytoBuoy [Dubelaar et al., 1999], FlowCytoBot [Olson et al., 2003], and SeaFlow [Swalwell et al., 2011] have provided an unprecedented view of dynamics of phytoplankton across large temporal and spatial scales.

Automated in-situ flow cytometry data can be represented as a scatterplot-valued time series, $\mathbf{y}^{(1)}, \dots, \mathbf{y}^{(T)}$, where an n_t by d matrix $\mathbf{y}^{(t)}$ whose rows are vectors $\{\mathbf{y}_i^{(t)} \in \mathbb{R}^d : i = 1, \dots, n_t\}$ is called a *cytogram* and can be thought of as a d -dimensional scatterplot representing n_t particles

observed during time interval t . The d dimensions of the scatterplot represent d optical properties that are useful in distinguishing different cell types from each other. Figure 1 shows an example of three cytograms collected by SeaFlow in June 2017 during a two-week cruise conducted in the Northeast Pacific. With SeaFlow, cytograms are of dimension $d = 3$.

As apparent in the figure, the points within the cytograms display clear clustering structure. These different clusters correspond to cell populations of different types of phytoplankton. As the environmental conditions change, the populations change over time. In particular, in optical space, two noticeable phenomena over time are:

1. The number of cells in a given population can increase or decrease, with populations sometimes even appearing or disappearing entirely.
2. The centers of the cell populations are not fixed, but rather move over time.

Using expert knowledge and close manual inspection, oceanographers have been able to explain how some of these phenomena can be attributed to specific changes in environmental factors (e.g., oscillations in cell size due to sunlight and cell division) [Vaulot and Marie, 1999, Sosik et al., 2003, Ribalet et al., 2015].

Our goal is to develop a statistical approach for identifying how environmental factors can be predictive of changes to the cytograms. The promise of such a tool would be to discover new relationships between cell populations and environmental factors beyond those that may be known, or visible to the human eye.

Based on these observations and with this goal in mind, our statistical model for time-varying cytograms postulates a finite mixture model in which both the cluster probabilities and centers are allowed to vary over time. Changes to the cluster probabilities over time can capture the growing/shrinking and appearing/disappearing described above, while changes to the centers over time can capture the drifting/oscillating.

To be clear, our method does not explicitly incorporate the time (or space) aspect of the data. Instead, in our model, these cluster probabilities and centers are controlled by p time-varying covariates $\mathbf{X}^{(t)} \in \mathbb{R}^p$. While our model can accommodate features that are purely functions of time (e.g., $\sin t$, t^2 , spline basis functions, etc.), our focus here is on environmental covariates. Our analysis uses biological, physical, and chemical variables, shown in the bottom panel of Figure 1, that were retrieved from the Simons Collaborative Marine Atlas Project (CMAP) database (<https://simonscmmap.com>), which is a public database compiling various oceanographic data over space and time.

One key strength of our method is the *variable selection* property, allowing the analyst to identify the subset of covariates that are the strongest predictor of each cluster’s mean and probability movement over time. For instance, in Figure 2, the estimated coefficients reveal that higher sea surface temperature and lower phosphate can predict a decrease in probability of cluster E located in the lower-left corner, and time-lagged sunlight and nitrate well predict the horizontal and vertical movement of cluster E’s center.

Our framework represents a substantial improvement in the detail and richness of how this data can be modeled and analyzed. Flow cytometry data are traditionally analyzed by a technique called *gating*, which counts the number of cells falling into certain fixed, expert-drawn polygonal regions of \mathbb{R}^d corresponding to each cell population [Verschoor et al., 2015], reducing each scatterplot into several counts (giving the number of cells in each gated region) [Hyrkas et al., 2015]. Subjectivity in manual gating has been shown to be an obstacle to reproducibility [Hahne et al., 2009]. Furthermore, the presence of overlapping cell communities suggests that hard assignments to fixed disjoint regions may not be advisable. These and other shortcomings have led multiple authors to develop mixture model based approaches, as discussed in Aghaeepour et al. [2013]. While such models are an improvement over traditional gating, they do not naturally extend to oceanography in which we have a time series of cytograms. Naively, one might think one could get away with fitting a separate mixture model to each individual cytogram. However, doing so leaves one with the problem of

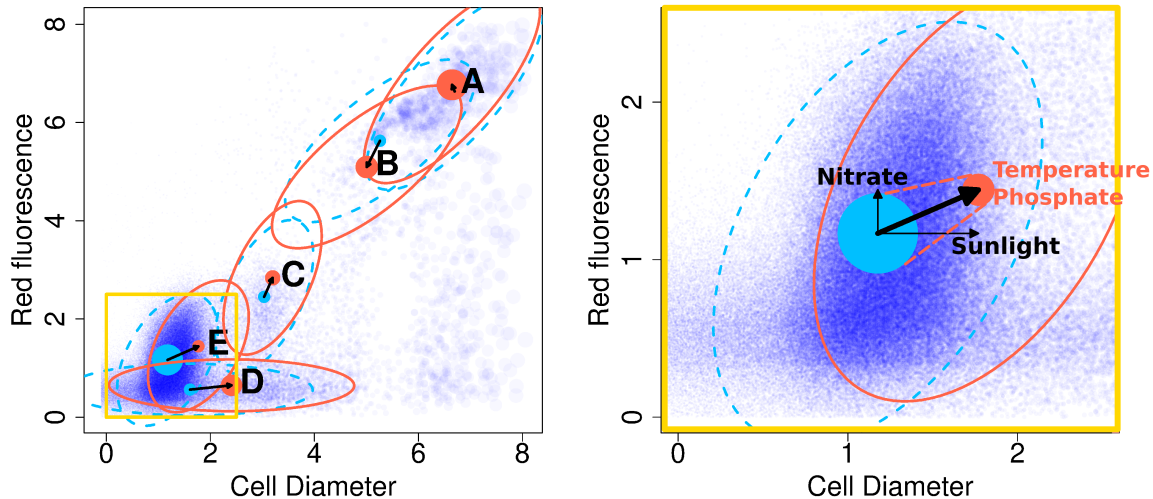


Figure 2: Our method produces estimates of cluster centers (shown as disks) and cluster probabilities (represented by the size of the disk) for every time point. The covariance of each mixture component (represented by an ellipse) is assumed to be constant over time. Blue and red show parameter estimates at two different time points. In the background, particles from only one time point are shown in (partially transparent) dark blue with the size of a point proportional to the particle’s biomass. The right figure takes a closer look at a subregion of the cytogram shown in the lower left corner of the left figure, focusing on cluster E which is a *Prochlorococcus* population. The change in the probability of cluster E is well predicted by sea surface temperature and phosphate, and the horizontal and vertical movement of cluster E’s center are each predicted by time-lagged sunlight and nitrate. Note, we are showing only five of the ten clusters used for estimation.

matching clusters from distinct clusterings, a task made particularly challenging since these clusters can move, change in size, and appear/disappear. Our approach fits a single mixture model *jointly* across the entire time series while integrating information from the covariates. By using all data sources in a single mixture model, our method is able to estimate the distinct components, even in cases where two populations’ centers may be nearby or a cluster may sometimes vanish.

In the statistics literature, the term *finite mixture of regressions* is used to refer to mixture models in which (univariate) means are modeled as functions of covariates (see, e.g., [McLachlan and Peel 2006](#)). Early works such as [Wang et al. \[1996\]](#) use information criteria and exhaustive search while more modern approaches have used penalized sparse models [[Khalili and Chen, 2007](#), [Städler et al., 2010](#)]. Our methodology differs from these methods in three respects: first, our means are multivariate (d -dimensional); second, the mixture weights are also modeled as functions of the covariates; third, the model coefficients are penalized. Of these, the first two aspects are shared by [Grün and Leisch \[2008\]](#), but without penalization. The idea of allowing the mixture weights to be functions of the features is more common in the machine learning literature, where such models are called *mixtures of experts* [[Jordan and Jacobs, 1993](#)].

To the best of our knowledge, this is the first attempt to extend mixture modeling of flow cytometry data by directly linking mixture model parameters with environmental covariates via sparse multivariate regression models. In Section 2, we describe our proposed model in detail. In section 3, we use our proposed model to draw rich new insights from a marine data source. We also conduct two realistic numerical simulations based on some pseudo-real ocean flow cytometry

data. We provide an R package called `flowmix` that can be run both on a single machine, and also on remote high performance servers that use a parallel computing environment. While our focus is on time-varying flow cytometry in the ocean, our method can be applied more broadly to any collection of cytograms with associated covariates. For example, in biomedical applications each cytogram could correspond to a blood sample from a different person, and person-specific covariates could model the variability in cytograms.

2 Methodology

2.1 Likelihood function of cytogram

We model the n_t particles $\{\mathbf{y}_i^{(t)}\}_{i=1}^{n_t}$ measured at time t as i.i.d. draws from a probabilistic mixture of K different d -variate Gaussian distributions, conditional on the covariate vector $\mathbf{X}^{(t)} \in \mathbb{R}^p$. The latent variable $Z_i^{(t)}$ determines the cluster membership,

$$P(Z_i^{(t)} = k | \mathbf{X}^{(t)}) = \pi_{kt}, \quad k = 1, \dots, K, \quad (1)$$

and the data is drawn from the k 'th Gaussian distribution,

$$(\mathbf{y}_i^{(t)} | \mathbf{X}^{(t)}, Z_i^{(t)} = k) \sim \mathcal{N}_d(\boldsymbol{\mu}_{kt}, \boldsymbol{\Sigma}_k),$$

where the cluster center $\boldsymbol{\mu}_{kt} \in \mathbb{R}^d$ and cluster probability π_{kt} at time t are modeled as functions of $\mathbf{X}^{(t)}$:

$$\begin{aligned} \boldsymbol{\mu}_{kt}(\beta) &= \boldsymbol{\beta}_{0k} + \boldsymbol{\beta}_k^T \mathbf{X}^{(t)} \\ \pi_{kt}(\alpha) &= \frac{\exp(\alpha_{0k} + \mathbf{X}^{(t)T} \boldsymbol{\alpha}_k)}{\sum_{l=1}^K \exp(\alpha_{0l} + \mathbf{X}^{(t)T} \boldsymbol{\alpha}_l)} \end{aligned}$$

for regression coefficients $\boldsymbol{\beta}_{0k} \in \mathbb{R}^d$, $\boldsymbol{\beta}_k \in \mathbb{R}^{p \times d}$, $\boldsymbol{\alpha}_k \in \mathbb{R}^p$, and $\alpha_{0k} \in \mathbb{R}$; throughout, we use α , β , and Σ to denote the collection of coefficients $\{\alpha_{0k}, \boldsymbol{\alpha}_k\}_{k=1}^K$, $\{\boldsymbol{\beta}_{0k}, \boldsymbol{\beta}_k\}_{k=1}^K$, and $\{\boldsymbol{\Sigma}_k\}_{k=1}^K$ for brevity. Since all random variables are conditional on the covariates $\mathbf{X}^{(t)}$, we will omit it hereon for brevity. Denoting the density of the k 'th Gaussian component of data at time t as $\phi(\cdot; \boldsymbol{\mu}_{kt}, \boldsymbol{\Sigma}^{(k)})$, the log-likelihood function is

$$\log \mathcal{L}(\alpha, \beta, \Sigma; \{\mathbf{y}_i^{(t)}\}_{i,t}) = \sum_{t=1}^T \sum_{i=1}^{n_t} \log \left(\sum_{k=1}^K \pi_{kt}(\alpha) \cdot \phi(\mathbf{y}_i^{(t)}; \boldsymbol{\mu}_{kt}(\beta), \boldsymbol{\Sigma}_k) \right). \quad (2)$$

By modeling the Gaussian means $\{\boldsymbol{\mu}_{kt}\}_{k,t}$ and mixture probabilities $\{\pi_{kt}\}_{k,t}$ as regression functions of $\mathbf{X}^{(t)}$ at each time point $t = 1, \dots, T$, our model directly allows environmental covariates to predict the two main kinds of cell population changes over time – movement in optical space, and change in relative population abundance. Furthermore, the signs and magnitudes of the entries of $\boldsymbol{\alpha}$ and $\boldsymbol{\beta}$ directly quantify the contribution of environment covariates to each population's abundance and direction of movement in cytogram space.

2.2 Penalties and constraints

In practice, there are a large number of environmental covariates that may in principle be predictive of a cytogram. Also, the number of regression parameters is $(p+1)(d+1)K$, which can be large relative to the number of cytograms T . Furthermore, we would prefer models in which only a small number of parameters is nonzero. Therefore, we penalize the log-likelihood with lasso penalties [Tibshirani, 1996] on α and β .

In our application, each cell population has a limited range in optical properties, due to biological constraints. We incorporate this domain knowledge into the model by constraining the range of $\boldsymbol{\mu}_{k1}, \dots, \boldsymbol{\mu}_{kT}$ over time. Since $\boldsymbol{\beta}_k^T \mathbf{X}^{(t)} = \boldsymbol{\mu}_{kt} - \boldsymbol{\beta}_{0k}$, limiting the size of $\boldsymbol{\beta}_k^T \mathbf{X}^{(t)}$ is equivalent to limiting the *deviation* of the k 'th cluster mean at all times $t = 1, \dots, T$ away from the overall center $\boldsymbol{\beta}_{0k}$. Motivated by this, we add a *hard* constraint so that $\|\boldsymbol{\beta}_k^T \mathbf{X}^{(t)}\|_2 \leq r$ for some fixed radius value $r > 0$.

The choice of r should be specific to the data application. For 1-dimensional cytograms of cell diameter measurements used in the analysis in Section 4.0.1, the size of r holds the intuitive meaning of not allowing the average optical properties of a particular cell population to deviate more than a multiplicative upper and lower bound over time compared to an overall average.

The constraint also plays an important role for model interpretability. We wish for the k 'th mixture component to correspond to the same cell population over all time. When a cell population vanishes we would like π_{kt} to go to zero rather than for $\boldsymbol{\mu}_{kt}$ to move to an entirely different place in cytogram space.

Our estimator is thus a solution to the following optimization problem:

$$\begin{aligned} \underset{\alpha, \beta, \Sigma}{\text{minimize}} \quad & -\frac{1}{N} \log \mathcal{L}(\alpha, \beta, \Sigma; \{\mathbf{y}_i^{(t)}\}_{i,t}) + \lambda_\alpha \sum_{k=1}^K \|\boldsymbol{\alpha}_k\|_1 + \lambda_\beta \sum_{k=1}^K \|\boldsymbol{\beta}_k\|_1. \\ \text{subject to} \quad & \|\boldsymbol{\beta}_k^T \mathbf{X}^{(t)}\|_2 \leq r \quad \forall t = 1, \dots, T \quad \forall k = 1, \dots, K. \end{aligned} \quad (3)$$

We divide the log-likelihood term by $N := \sum_{t=1}^T n_t$ to make the scale consistent with that of a single particle.

2.3 Multiplicity generalization

Cytogram datasets can be extremely large, and cell populations can have highly imbalanced probabilities. To overcome the computational and methodological difficulties posed by these issues, we generalize the model to assign to particle $\mathbf{y}_i^{(t)}$ a multiplicity factor $C_i^{(t)}$ (which defaults to 1). The log-likelihood in (2) becomes,

$$\ell_{(n_1, \dots, n_T)}(\alpha, \beta, \Sigma; (\mathbf{y}^{(1)}, \dots, \mathbf{y}^{(T)}), (\mathbf{C}^{(1)}, \dots, \mathbf{C}^{(T)})) = \sum_{t=1}^T \sum_{i=1}^{n_t} C_i^{(t)} \log \left(\sum_{k=1}^K \pi_{kt}(\alpha) \cdot \phi(\mathbf{y}_i^{(t)}; \boldsymbol{\mu}_{kt}(\beta), \boldsymbol{\Sigma}_k) \right). \quad (4)$$

where $\mathbf{y}^{(t)} \in \mathbb{R}^{n_t \times d}$ and $\mathbf{C}^{(t)} \in \mathbb{R}^{n_t}$. Furthermore, the scaling by N in the optimization objective (3) is generalized to $N := \sum_{t=1}^T \sum_{i=1}^{n_t} C_i^{(t)}$, the overall sum of the multiplicities.

The multiplicity generalization is useful for an approximate data representation by placing particles in bins and dealing with bin counts. We discretize cytogram space along a lattice of $B = D^d$ d -dimensional cubes $\{E_b\}_{b=1}^B$ whose centers $\tilde{\mathbf{y}}_b \in \mathbb{R}^d$ can be arranged as the rows of a matrix $\tilde{\mathbf{y}} \in \mathbb{R}^{B \times d}$. This coarsened data representation involves counts $\{C_b^{(t)}\}_{b,t}$ of the number of particles in each fixed bin E_b :

$$C_b^{(t)} = \sum_{i=1}^{n_t} \mathbb{1}\{i : \mathbf{y}_i^{(t)} \in E_b\},$$

whose collection is $\mathbf{C}^{(t)} \in \mathbb{R}^B$. Using $C_b^{(t)}$ and $\tilde{\mathbf{y}}_b^{(t)} := \tilde{\mathbf{y}}_b$ to replace $C_i^{(t)}$ and $\mathbf{y}_i^{(t)}$ in (4), we obtain

the log-likelihood of the binned data,

$$\begin{aligned} \ell_{(B, \dots, B)} \left(\alpha, \beta, \Sigma; (\tilde{\mathbf{y}}, \dots, \tilde{\mathbf{y}}), (\mathbf{C}^{(1)}, \dots, \mathbf{C}^{(T)}) \right) \\ = \sum_{t=1}^T \sum_{b=1}^B C_b^{(t)} \log \left(\sum_{k=1}^K \pi_{kt}(\alpha) \cdot \phi(\tilde{\mathbf{y}}_b; \boldsymbol{\mu}_{kt}(\beta), \boldsymbol{\Sigma}_k) \right). \end{aligned} \quad (5)$$

Whereas before each cytogram required its own set of n_t particle locations, in the binned data representation, the same set of locations are shared across all t , which is indicated by the notation $(\tilde{\mathbf{y}}, \dots, \tilde{\mathbf{y}})$.

This binned likelihood is identical to the original log-likelihood (2) after replacing each particle by its bin center. The computational savings are apparent from noticing that $\sum_{b=1}^B \mathbf{1}\{C_b^{(t)} \neq 0\} \ll n_t$ since typically only a small subset of the bins $\{E_b\}$ contain any particles. Additionally, the number of Gaussian density calculations are reduced by a factor of T , since the particles $\tilde{\mathbf{y}}_b$ do not depend on t .

There is no finite value of B for which the binned log-likelihood in (5) is equal to the log-likelihood calculated on the original data, due to the nonzero distance between bin centers $\tilde{\mathbf{y}}_b$ and data $\mathbf{y}_i^{(t)}$ even for very large B . However, the following proposition 1 establishes that parameter estimation from the binned data is asymptotically equivalent to parameter estimation from the original data, as the number of bins B grows to ∞ . The proof is provided in Supplement A. As for what occurs for finite values of B , a simulation study in Supplement F suggests that even using a relatively small number of bins can achieve similar predictive performance as using the original data.

Proposition 1. Let

$$\tilde{\Theta}_B := \operatorname{argmin}_{(\alpha, \beta, \Sigma) \in \Theta} -\frac{1}{N} \ell_{(B, \dots, B)} \left(\alpha, \beta, \Sigma; (\tilde{\mathbf{y}}, \dots, \tilde{\mathbf{y}}), (\mathbf{C}^{(1)}, \dots, \mathbf{C}^{(T)}) \right) + g(\alpha, \beta) \quad (6)$$

be the set of minimizers of the penalized negative log-likelihood of the binned data, and let

$$\hat{\Theta} := \operatorname{argmin}_{(\alpha, \beta, \Sigma) \in \Theta} -\frac{1}{N} \log \mathcal{L}(\alpha, \beta, \Sigma; \{\mathbf{y}_i^{(t)}\}_{i,t}) + g(\alpha, \beta), \quad (7)$$

be that of the original data. The term $g(\alpha, \beta)$ encapsulates the penalties on α and β and the constraint on β in (3). Assume the following:

1. The parameter space Θ of (α, β, Σ) is compact, and $\{\lambda_{\min}(\boldsymbol{\Sigma}_k) < c\} \cap \Theta = \emptyset$ for all $k = 1, \dots, K$, for some constant $c > 0$.
2. The data belongs to a compact set \mathcal{Y} with $\max_{\mathbf{y}, \mathbf{y}' \in \mathcal{Y}} \|\mathbf{y} - \mathbf{y}'\|_{\infty} \leq R$ for some positive constant $R < \infty$.
3. The log likelihood $\log \mathcal{L}(\alpha, \beta, \Sigma; \{\mathbf{y}_i^{(t)}\}_{i,t}) < \infty$ for all $(\alpha, \beta, \Sigma) \in \Theta$.

Then, given any sequence $\tilde{\theta}_B \in \tilde{\Theta}_B (B = 1, 2, \dots)$ of minimizers of the penalized negative log-likelihood of the binned data, a sequence s_B exists such that the subsequence $\tilde{\theta}_{s_B}$ converges to an element in $\hat{\Theta}$:

$$\lim_{B \rightarrow \infty} \tilde{\theta}_{s_B} \in \hat{\Theta}. \quad (8)$$

This generalization to a binned data representation can be thought of as trading off some data resolution for significant computational savings in practice. To illustrate, the entire set of 3d particles collected during the Gradients 2 cruise, divide into about $T = 300$ hourly cytograms containing $n_t \simeq 100,000$ particles each. This occupies $d \cdot \sum_{t=1}^T n_t$ doubles, or 800 Mb in memory for $d = 3$. Equally burdensome is the size of the responsibilities $\{\gamma_{itk}\}_{i,t,k}$ (to be defined shortly in Section 2.4)

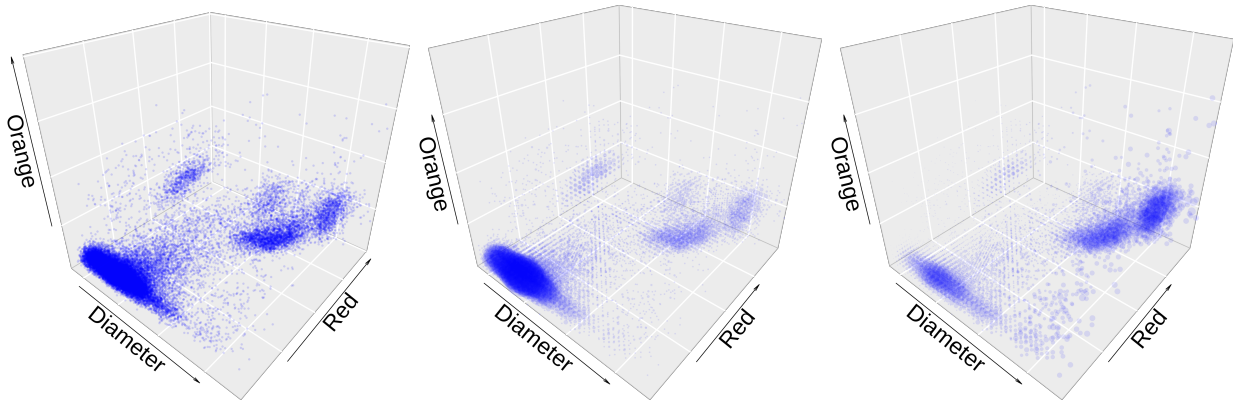


Figure 3: *Original particles (left) and binned counts with $D = 40$ (middle), and binned biomass (right). In the middle and right plots, the size of the points are proportional to the multiplicity. The left-hand-side original cytogram contain one hour’s worth of particles, for a total of $n_t = 36,757$ points, occupying a total of 0.86 Mb of memory. The binned cytogram in the middle occupies about 1/8th the memory. The right hand side shows binned biomass data, which has lesser imbalance in cluster distribution than the binned count data in the middle.*

and densities of each particle with respect to all K clusters, which are each $\sum_t(n_t \cdot K \cdot d)$ doubles, or 2.5 Gb in memory for $K = 10$. By contrast, when binned with $D = 40$, this becomes 40 Mb in memory.

The *biomass* representation of data uses carbon quotas – the amount of carbon in each particle, in pgC per cell – $C_i^{(t)} := \text{Biomass}(\mathbf{y}_i^{(t)})$, instead of repeated particle counts as multiplicities, and the *binned* biomass representation of data aggregates the total carbon biomass in each bin, as $C_b^{(t)} = \sum_{i:i \in A_b^{(t)}} \text{Biomass}(\mathbf{y}_i^{(t)})$. The data analysis in our paper uses the binned biomass representation.

From a modeling viewpoint, the carbon biomass representation is an attractive alternative to the particle count representation because our cytograms have highly imbalanced particle clusterings, a setting in which mixture models generally perform poorly [Xu and Jordan, 1996]. From a biogeochemical standpoint, biomass distributions are meaningful since cell count is usually inversely proportional to particle size: small cells tend to dominate numerically the ocean due to their smaller size and lesser expenditure of biochemical resources [Marañón, 2015].

However, representing data with biomass is not without complication. Using biomass as multiplicities requires an additional assumption that carbon atoms can be treated in the same way we have treated particles. However, we know that carbon atoms arrive in bundles (according to particle sizes) and therefore treating them as independent is an unrealistic assumption. That said, in practice, we see that this simplifying assumption still produces useful and interpretable estimated models.

2.4 Penalized Expectation-Maximization Algorithm

Directly maximizing the penalized log-likelihood (3), generalized with multiplicities, is difficult due to its nonconvexity. We outline a *penalized* EM algorithm [Pan and Shen, 2007] for indirectly maximizing the objective.

Recall from (1) that latent variable $Z_i^{(t)}$ encodes the particle’s cluster membership:

$$Z_i^{(t)} \in \{1, \dots, K\}.$$

Also define the joint log-likelihood of the data and the latent variables to be:

$$\begin{aligned} \log \mathcal{L}_c(\alpha, \beta, \Sigma; \{\mathbf{y}_i^{(t)}\}_{i,t}, \{Z_i^{(t)}\}_{i,t}, \{C_i^{(t)}\}_{i,t}) \\ = \sum_{t=1}^T \sum_{i=1}^{n_t} C_i^{(t)} \sum_{k=1}^K \mathbb{1}\{Z_i^{(t)} = k\} \cdot \log \left(\pi_{kt}(\alpha) \cdot \phi(\mathbf{y}_i^{(t)}; \boldsymbol{\mu}_{kt}(\beta), \boldsymbol{\Sigma}_k) \right). \end{aligned} \quad (9)$$

Now, denote the conditional probability of membership as:

$$\gamma_{itk}(\alpha, \beta, \Sigma) = \mathbb{P}_{\alpha, \beta, \Sigma}(Z_i^{(t)} = k | \mathbf{y}^{(t)}, \mathbf{X}^{(t)}),$$

sometimes called *responsibilities* in the literature.

Given some latest estimates of the parameters $(\hat{\alpha}, \hat{\beta}, \hat{\Sigma})$, we make use of the surrogate objective $Q(\alpha, \beta, \Sigma | \hat{\alpha}, \hat{\beta}, \hat{\Sigma})$ defined as the penalized conditional expectation (in terms of the conditional distribution of $Z^{(t)} | \mathbf{y}^{(t)}, \mathbf{X}^{(t)}$) of the joint penalized log-likelihood,

$$\begin{aligned} Q(\alpha, \beta, \Sigma | \hat{\alpha}, \hat{\beta}, \hat{\Sigma}) = \frac{1}{N} \sum_{t=1}^T \sum_{i=1}^{n_t} C_i^{(t)} \sum_{k=1}^K \gamma_{itk}(\hat{\alpha}, \hat{\beta}, \hat{\Sigma}) \log \left(\pi_{kt}(\alpha) \cdot \phi(\mathbf{y}_i^{(t)}; \boldsymbol{\mu}_{kt}(\beta), \boldsymbol{\Sigma}_k) \right) \\ - \lambda_\alpha \sum_{k=1}^K \|\boldsymbol{\alpha}_k\|_1 - \lambda_\beta \sum_{k=1}^K \|\boldsymbol{\beta}_k\|_1 - \sum_{k=1}^K \sum_{t=1}^T \mathbb{1}_{\infty} \{ \|\boldsymbol{\beta}_k^T \mathbf{X}^{(t)}\|_2 \leq r \}. \end{aligned} \quad (10)$$

The algorithm alternates between estimating the conditional membership probabilities γ_{itk} , and updating the latest parameter estimates $(\hat{\alpha}, \hat{\beta}, \hat{\Sigma})$ by the maximizer of the penalized Q function in (10).

1. **E-step** Given $(\hat{\alpha}, \hat{\beta}, \hat{\Sigma})$, estimate the conditional membership probabilities as

$$\gamma_{itk}(\hat{\alpha}, \hat{\beta}, \hat{\Sigma}) = \frac{\phi(\mathbf{y}_i^{(t)}; \boldsymbol{\mu}_{kt}(\hat{\beta}), \hat{\Sigma}_k) \cdot \pi_{kt}(\hat{\alpha})}{\sum_{l=1}^L \phi(\mathbf{y}_i^{(t)}; \boldsymbol{\mu}_{lt}(\hat{\beta}), \hat{\Sigma}_l) \cdot \pi_{lt}(\hat{\alpha})}, \quad (11)$$

for $k = 1, \dots, K; t = 1, \dots, T; i = 1, \dots, n_t$. For the first iteration, choose some initial values for means $\boldsymbol{\mu}_{kt} \leftarrow \boldsymbol{\mu}_k^{\text{init}}$, probabilities $\pi_{kt} \leftarrow 1/K$, and $\hat{\Sigma}_k \leftarrow \boldsymbol{\Sigma}_k^{\text{init}} = g\mathbf{I}_d$ for some constant $g > 0$.

2. **M-step** Using $\gamma_{itk} = \gamma_{itk}(\hat{\alpha}, \hat{\beta}, \hat{\Sigma})$, maximize (10) with respect to each parameter α, β and Σ :
 - (a) **Update $\hat{\alpha}$:** The maximizer of (10) with respect to α is

$$\begin{aligned} \hat{\alpha} \leftarrow \operatorname{argmax}_{\{\boldsymbol{\alpha}_k\}_{k=1}^K} \frac{1}{N} \sum_{t=1}^T \left(\sum_{k=1}^K \gamma_{tk}(\alpha_{0k} + \mathbf{X}^{(t)T} \boldsymbol{\alpha}_k) - n_t \log \sum_{l=1}^K \exp(\alpha_{0l} + \mathbf{X}^{(t)T} \boldsymbol{\alpha}_l) \right) \\ - \lambda_\alpha \sum_{k=1}^K \|\boldsymbol{\alpha}_k\|_1 \end{aligned}$$

for sums $\gamma_{tk} = \sum_{i=1}^{n_t} C_i^{(t)} \gamma_{itk}$.

- (b) **Update $\hat{\beta}$:** Update β according to the ADMM algorithm described in Section 2.5 and Supplement B. Since the problem decouples across clusters, we solve separately for each k :

$$\begin{aligned} (\hat{\beta}_{0k}, \hat{\beta}_k) \leftarrow \operatorname{argmin}_{\beta_{0k}, \beta_k} \frac{1}{2N} \sum_{t=1}^T \sum_{i=1}^{n_t} C_i^{(t)} \gamma_{itk}(\mathbf{y}_i^{(t)} - \beta_{0k} - \beta_k^T \mathbf{X}^{(t)})^T \hat{\Sigma}_k^{-1} (\mathbf{y}_i^{(t)} - \beta_{0k} - \beta_k^T \mathbf{X}^{(t)}) \\ + \lambda_\beta \|\boldsymbol{\beta}_k\|_1 \\ \text{subject to } \|\boldsymbol{\beta}_k^T \mathbf{X}^{(t)}\|_2 \leq r \quad \forall t = 1, \dots, T. \end{aligned}$$

(c) **Update $\hat{\Sigma}$** : The maximizer of (10) with respect to Σ_k for each $k = 1, \dots, K$ is

$$\hat{\Sigma}_k \leftarrow \frac{\sum_{t=1}^T \sum_{i=1}^{n_t} C_i^{(t)} \gamma_{itk} \cdot \mathbf{r}_{itk} \mathbf{r}_{itk}^T}{\sum_{t=1}^T \sum_{i=1}^{n_t} C_i^{(t)} \gamma_{itk}}$$

$$\text{for } \mathbf{r}_{itk} = \mathbf{y}_i^{(t)} - \hat{\beta}_{0k} - \hat{\beta}_k^T \mathbf{X}^{(t)}.$$

Note, the M-step breaks into a convex problem over α (step 2a) and a non-convex problem over (β, Σ) (step 2b and 2c). For the latter part of the M-step, instead of jointly optimizing over (β, Σ) , we perform two successive partial optimizations – first with respect to β , and next, with respect to Σ .

This algorithm is terminated when the penalized log-likelihood has a negligible relative improvement. In practice, we run the EM algorithm multiple times and retain the run with the highest final log-likelihood, for a better chance at achieving the true optimum. For μ_k^{init} we randomly choose K out of all $\sum_{t=1}^T n_t$ cytogram particles. Initial covariances $\{\Sigma_k^{\text{init}}\}_{k=1}^K$ are set to have diagonal entries g equal to $1/K$ times the cytogram range in each dimension. The α part of the M-step is solved using `glmnet`, with `family` set to ‘‘multinomial’’ [Friedman et al., 2010]. The β part of the M-step requires a custom alternating direction method of multipliers (ADMM) solver, outlined in the next section.

2.5 ADMM algorithm in M-step for β

The β M-step (in step b) is very slow if computed using a non-customized solver – for instance, using CVX [Grant and Boyd, 2014], it is the slowest component of the EM algorithm by a factor of ten or more. To improve performance, we devise a customized alternating direction method of multipliers (ADMM) algorithm [Boyd et al., 2011]. We start by observing that this optimization problem decouples across k . Since each $k \in \{1, \dots, K\}$ can be solved separately, we will drop the subscript k hereon and write the variables β_{0k} and β_k as β_0 and β , γ_{itk} as γ_{it} , and $\hat{\Sigma}_k$ as $\hat{\Sigma}$ for notational simplicity.

Consider the minimization problem in step b of the M-step of the penalized EM algorithm. The objective to minimize can be written as

$$f(\beta_0, \beta) = \frac{1}{2N} \sum_{i,t} C_i^{(t)} \gamma_{it} (\mathbf{y}_i^{(t)} - \beta_0 - \beta^T \mathbf{X}^{(t)})^T \hat{\Sigma}^{-1} (\mathbf{y}_i^{(t)} - \beta_0 - \beta^T \mathbf{X}^{(t)}) + \lambda_\beta \|\beta\|_1 + \mathbf{1}_\infty \{\|\beta^T \mathbf{X}^{(t)}\|_2 \leq r\}.$$

We can obtain the overall minimizer via partial minimization with respect to β_0 ; writing $\hat{\beta}_0(\beta) := \text{argmin}_{\beta_0} f(\beta_0, \beta)$ for this partial minimizer, setting the gradient to 0 yields a closed form expression of $\hat{\beta}_0(\beta) = \frac{\sum_{i,t} C_i^{(t)} \gamma_{it} (\mathbf{y}_i^{(t)} - \beta^T \mathbf{X}^{(t)})}{\sum_{i,t} C_i^{(t)} \gamma_{it}}$. The objective to minimize with respect to β then becomes

$$f(\hat{\beta}_0(\beta), \beta) = \frac{1}{2N} \sum_{i,t} C_i^{(t)} \gamma_{it} (\tilde{\mathbf{y}}_i^{(t)} - \beta^T \tilde{\mathbf{X}}^{(t)})^T \hat{\Sigma}^{-1} (\tilde{\mathbf{y}}_i^{(t)} - \beta^T \tilde{\mathbf{X}}^{(t)}) + \lambda_\beta \|\beta\|_1 + \mathbf{1}_\infty \{\|\beta^T \tilde{\mathbf{X}}^{(t)}\|_2 \leq r\},$$

where $\tilde{\mathbf{y}}^{(t)} := \mathbf{y}_i^{(t)} - \bar{\mathbf{y}}$ and $\tilde{\mathbf{X}}^{(t)} := \mathbf{X}^{(t)} - \bar{\mathbf{X}}$ are data centered by weighted averages $\bar{\mathbf{y}} := \sum_{i,t} C_i^{(t)} \gamma_{it} \mathbf{y}_i^{(t)} / \sum_{i,t} C_i^{(t)} \gamma_{it}$ and $\bar{\mathbf{X}} := \sum_{i,t} C_i^{(t)} \gamma_{it} \mathbf{X}^{(t)} / \sum_{i,t} C_i^{(t)} \gamma_{it}$. Now, introducing augmented variables $\mathbf{Z} \in \mathbb{R}^{T \times d}$ and $\mathbf{W} \in \mathbb{R}^{p \times d}$, we can rewrite $\min_{\beta} f(\hat{\beta}_0(\beta), \beta)$ as:

$$\begin{aligned} & \underset{\beta, \mathbf{Z}, \mathbf{W}}{\text{minimize}} && \frac{1}{2N} \sum_{i,t} C_i^{(t)} \gamma_{it} (\tilde{\mathbf{y}}_i^{(t)} - \beta^T \tilde{\mathbf{X}}^{(t)})^T \hat{\Sigma}^{-1} (\tilde{\mathbf{y}}_i^{(t)} - \beta^T \tilde{\mathbf{X}}^{(t)}) + \lambda \|\mathbf{W}\|_1 \\ & \text{subject to} && \|\mathbf{Z}^{(t)}\|_2 \leq r, \\ & && \begin{pmatrix} \mathbf{X} \\ \mathbf{I} \end{pmatrix} \beta = \begin{pmatrix} \mathbf{Z} \\ \mathbf{W} \end{pmatrix}, \end{aligned} \tag{12}$$

which can be solved using an ADMM whose full details are deferred to Supplement B. All steps are computationally simple, consisting of least squares reduced to rapidly solvable Sylvester equations, ℓ_2 ball projection, and soft-thresholding. The implementation in the `flowmix` R package is highly optimized and faster than any other component of the EM algorithm.

2.6 Cross-validation for selection of λ_α , λ_β

We choose the regularization parameter values $(\lambda_\alpha, \lambda_\beta)$ using five-fold cross-validation over a discrete 2-dimensional grid of candidate values $L_\alpha \times L_\beta$, in which L_α and L_β each contain logarithmically-spaced positive real numbers. We form the five folds consisting of every fifth time block containing 20 consecutive time points. Denote these five test folds' time points as sets $\{I_o\}_{o=1}^5$, so that $I_1 = \{1, \dots, 20, 101, \dots, 120, \dots\}$, $I_2 = \{21, \dots, 40, 121, \dots, 140, \dots\}$, and so forth. Writing $I_{-o} = \{1, \dots, T\} \setminus I_o$, the test datasets comprise of the subsetted data $\{(\mathbf{X}_o, \mathbf{y}_o, \mathbf{C}_o)\}_{o=1}^5$ for $\mathbf{X}_o := \{\mathbf{X}^{(t)} : t \in I_o\}$, $\mathbf{y}_o := \{\mathbf{y}^{(t)} : t \in I_o\}$ and $\mathbf{C}_o := \{\mathbf{C}^{(t)} : t \in I_o\}$, and the corresponding training dataset comprise of $\{(\mathbf{X}_{-o}, \mathbf{y}_{-o}, \mathbf{C}_{-o})\}_{o=1}^5$.

The five-fold cross-validation score is calculated as the average of the out-of-sample negative log-likelihood in (4):

$$S(\lambda_\alpha, \lambda_\beta) = -\frac{1}{5} \sum_{o=1}^5 \ell_{\{n_t: t \in I_o\}}(\hat{\alpha}_{-o}, \hat{\beta}_{-o}, \hat{\Sigma}_{-o}; \mathbf{y}_o, \mathbf{X}_o, \mathbf{C}_o),$$

where $\hat{\alpha}_{-o}$, $\hat{\beta}_{-o}$ and $\hat{\Sigma}_{-o}$ are the estimated coefficients from the training data set $(\mathbf{X}_{-o}, \mathbf{y}_{-o}, \mathbf{C}_{-o})$. (We include \mathbf{X}_o in $\ell(\cdot)$ to emphasize which subset of the covariates the log-likelihood is based on.) The cross-validated regularization parameter values λ_α and λ_β are the minimizer of the cross-validation score:

$$(\hat{\lambda}_\alpha, \hat{\lambda}_\beta) = \underset{\lambda_\alpha \in L_\alpha, \lambda_\beta \in L_\beta}{\operatorname{argmin}} S(\lambda_\alpha, \lambda_\beta).$$

A real data example of cross-validation scores in action is shown in Figures 12 and 13 in the Supplement. Our scheme of training/test splits places a strong emphasis on even temporal coverage of the test data. Since our data are in hourly resolution (equivalent to 20 kilometers in space) and cross-validation folds are made of 20-hour-long time blocks, the temporal closeness of the test time points I_o and the training time points I_{-o} is negligible. For data with finer time resolution, our recommendation is to form a time *barrier* between the training and test time points, or to form larger time blocks for test folds. Also, in this work, we do not discuss how to select the number of clusters K based on data. In simulation, we demonstrate that slightly overspecifying the number of clusters results in equivalent predictive performance as the true number of clusters. See Section 3.1.2 for details.

3 Numerical results

3.1 Simulated data

In order to examine the numerical properties of our proposed method, we apply our model to simulated data whose setup is closely related to our main flow cytometry datasets.

3.1.1 Noisy covariates

The main source of noise in our data is in the environmental covariates from a variety of sources – in-situ and remote-sensing measurements, and oceanographic model-derived product [Boyer et al., 2013], each with different temporal and spatial resolution, and varying amounts of uncertainties. In order to investigate the effect of uncertainty in the covariates, we conduct a simulation in which

synthetic cytograms are generated from a true model and underlying covariates, and then our model is estimated with access to only artificially obscured covariates.

We generate synthetic data with $T = 100$ time points, $K = 2$ clusters, and $p = 10$ covariates $\{X_i \in \mathbb{R}^T\}_{i=1}^{10}$ as shown in Figure 4 – one sunlight variable \mathbf{X}_1 , one changepoint variable \mathbf{X}_2 , and eight spurious covariates $\{\mathbf{X}_i\}_{i=3}^{10}$. From these covariates, T 1-dimensional cytograms are generated from the generative model in Section 2.1 with the true underlying coefficient values,

$$\begin{aligned} \alpha_{0,1} = 0, \quad \alpha_{0,2} = 0, \quad \boldsymbol{\alpha}_1 = (0 \ 0 \ \cdots \ 0)^T, \quad \boldsymbol{\alpha}_2 = (0 \ 8.61 \ \cdots \ 0)^T, \\ \beta_{0,1} = 0, \quad \beta_{0,2} = 3, \quad \boldsymbol{\beta}_1 = (0.3 \ 0 \ \cdots \ 0)^T, \quad \boldsymbol{\beta}_2 = (-0.3 \ 0 \ \cdots \ 0)^T. \end{aligned} \quad (13)$$

Both clusters’ means follow the sunlight \mathbf{X}_1 . Cluster 1 has $n_t = 200$ particles for all time points $t = 1, \dots, 100$. Cluster 2 overlaps with cluster 1, is present only in the second half of the time range $t = 51, \dots, 100$, and is 1/4th as populous as cluster 1 at those time points. Both cluster variances are equal to 1 so that particles from each cluster are generated from $\mathcal{N}(0, 1)$ around their respective means, and the spurious covariates play no role in data generation i.e. all other coefficients not specified in (13) are zero.

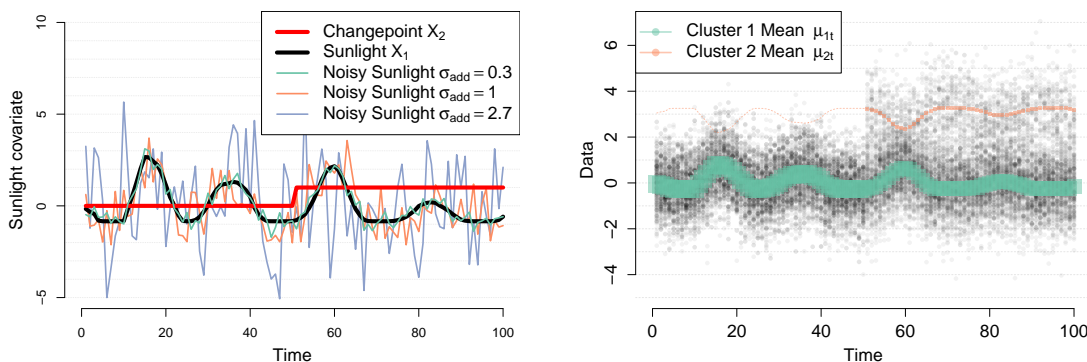


Figure 4: (Left) The thick black line shows the first covariate $\mathbf{X}_1 \in \mathbb{R}^T$, which is a smoothed and standardized version of the *par* (sunlight) covariate from Section 4.0.1. The three thin lines show the obscured sunlight variables for three different noise levels σ_{add} . The next covariate is a changepoint variable $\mathbf{X}_2 \in \mathbb{R}^T$, shown as a thick red line. The remaining 8 spurious covariates $\{\mathbf{X}_i\}_{i=3}^{10}$ are generated as T i.i.d. entries from $\mathcal{N}(0, 1 + \sigma_{\text{add}}^2)$; these are not shown here. (Right) An example of a generated dataset, whose particles are shown as grey points in the background. The two true cluster means are plotted as colored lines whose thickness is proportional to the cluster probabilities. Particles for both clusters are generated as $\mathcal{N}(0, 1)$ around the cluster means. Cluster 1 is only present in the second half, and has one quarter of the number of particles in cluster 2 in those time points. A thin dashed line is shown in the first half where the cluster probability is zero.

On each new synthetic dataset, we estimate a cross-validated 2-cluster model using radius $r = 1.5$, but instead of sunlight covariate \mathbf{X}_1 , we use the *obscured* $\mathbf{X}_1^{\text{noisy}} = \mathbf{X}_1 + \boldsymbol{\epsilon}$, $\boldsymbol{\epsilon} \sim \mathcal{N}(0, \sigma_{\text{add}}^2 \mathbf{I}_T)$ for estimation. Also, the eight spurious covariates $\{\mathbf{X}_i\}_{i=3}^{10}$ are each generated as $\mathcal{N}(0, 1 + \sigma_{\text{add}}^2)$ to match the magnitude of $\mathbf{X}_1^{\text{noisy}}$. We consider a certain range of additive noise $\sigma_{\text{add}} \in \{0, 0.3, 0.6, \dots, 2.7\}$, and 100 synthetic datasets for each value σ_{add} .

The left plot of Figure 5 shows the out-of-sample model prediction performance of 100 estimated models for each noise level σ_{add} , measured as the negative log likelihood evaluated on a large independent test dataset. As expected, out-of-sample prediction gradually worsens with increasing covariate noise σ_{add} , then plateaus at about $\sigma_{\text{add}} = 2.7$.

The right plot of Figure 5 demonstrates the variable selection property of our method, focusing on the β coefficients. Focusing on the sunlight variable – the only true predictor of mean movement

– we see that it is more likely to be selected than are spurious covariates, and is less likely to be selected as σ_{add} increases. Additionally, we see that selecting sunlight is possible even when σ_{add} is high if the cluster has higher relative probability and has nonzero probability in a longer time range.

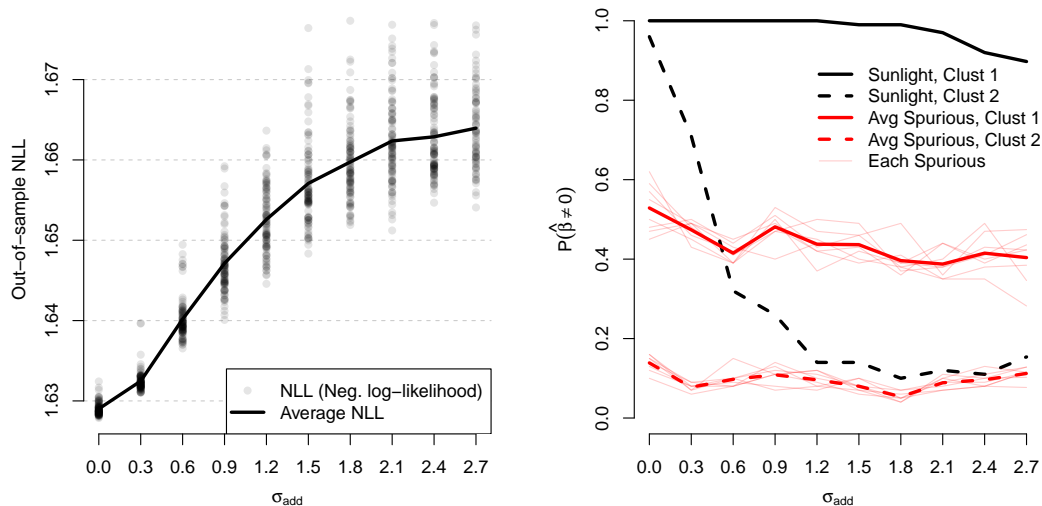


Figure 5: (Left) Out-of-sample prediction performance using covariates obscured by Gaussian noise variance σ_{add}^2 , for the simulation setup described in Section 3.1.1. (Right) The probability of the sunlight covariate (the only relevant covariate for cluster means) being estimated as nonzero is shown in black lines. The corresponding probabilities for the eight spurious covariates are shown in red lines (thin red lines are individual covariates, and the thick red line is the average). The solid and dashed lines show results from cluster 1 and cluster 2 respectively. In both clusters, the sunlight variable is more likely to be selected than the spurious variables. This advantage is more pronounced for cluster 1 than for cluster 2, which is only has data in the second half of the time range.

3.1.2 Cluster number misspecification

In addition to covariate noise, we explore the effect of misspecifying the number of clusters K in the model. We first form a ground truth model by taking the five-cluster estimated model from the 1-dimensional $T = 296$ data in Section 4.0.1 and Figure 7, and zero-thresholding the smaller estimated coefficients. We then generate new data 30 times from this underlying true model, and estimate a K -cluster cross-validated model, for $K \in \{2, 3, 4, 5, 6, 7, 8\}$. Figure 6 shows out-of-sample prediction performance, measured as the negative log-likelihood on a large independent test set generated from the true model. We see that models estimated with $K < 5$ clusters have sharply deteriorating out-of-sample prediction. On the other hand, models estimated with $K > 5$ than five clusters have average out-of-sample prediction performance in the same range as that of $K = 5$ cluster models. A closer examination of the estimated models reveals that, out of the $K > 5$ clusters, five clusters are usually estimated accurately, and the remaining $K - 5$ clusters are estimated with near-zero probability. These results suggest that one can slightly overspecify the number of clusters for estimation with little harm to prediction performance. Automatic approaches to choosing K is an interesting area of future work.

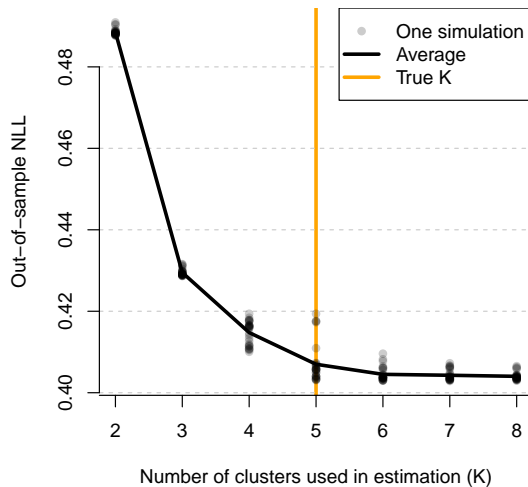


Figure 6: *Out-of-sample prediction performance for K -cluster models estimated from 5-cluster pseudo-real datasets (which were each generated from a simplified version of a model estimated from real 1-dimensional data, in Section 4.0.1). Models estimated with fewer than 5 clusters have sharply worse out-of-sample prediction performance. On the other hand, estimated models with 5 clusters or more have similar out-of-sample prediction performance, because the extra clusters are estimated to have zero probability, and play no role in the prediction.*

4 Application to Seaflo cruise

In this section, we apply our model to data collected on a research cruise in the North Pacific Ocean, and from the Simons CMAP database (<https://simonscmmap.com/>). The MGL1704 cruise traversed two oceanographic regions over the course of about 2 weeks, between dates 2017-05-28 and 2017-06-13. As seen in Figure 1, the cruise started in the North Pacific Subtropical Gyre (low latitude, dominated by warm, saltier water), traveling north to the Subpolar Gyre (high latitude, low-temperature, low-salt, nutrient-rich water), and returned back south. We first describe the data and model setup, then discuss the results.

Environmental covariates. A total of 33 environment covariates (see Table 1 and Figure 11 of the Supplement) were *colocalized* with cytometric data by averaging the environmental data measurements within a rectangle of every discrete point of the cruise trajectory in space and time, aggregated to an hourly resolution. These data were processed and downloaded from the Simons CMAP database [Ashkezari et al., 2021] accessed through the CMAP4R R package [Hyun et al., 2020]. In addition to these covariates, we created four new covariates by lagging the sunlight covariate in time by $\{3, 6, 9, 12\}$ hours. This was motivated by scientific evidence showing that the peak of phytoplankton cell division is out of phase with sunlight [Ribalet et al., 2015]. We also created two new changepoint variables demarcating the two crossings events of the cruise through a biological transition line at latitude 37. These derived covariates play the role of allowing a more flexible *conditional* representation of the cytograms, using information from the covariates. All covariates except for the two changepoint variables were centered and scaled to have sample variance of 1. Altogether, we formed a covariate matrix $\mathbf{X} \in \mathbb{R}^{(308-12) \times 39}$. (The first twelve time points are deleted due to the lagging of the sunlight variable.)

Response data (cytograms). The response data (cytograms) were collected on-board using

a continuous-time flow cytometer called SeaFlow, which continuously analyzes sea water through a small opening and measures the optical properties of individual microscopic particles [Swalwell et al., 2011]. The data consist of measurements of light scatter and fluorescence emissions of individual particles. Data are organized into files recorded every 3 minutes, where each file contains measurements of the cytometric characteristics of between 1,000 and 100,000 particles ranging from 0.5 to 5 microns in diameter. The size of data in any given file depends on the cell abundance of phytoplankton within the sampled region. Each particle is characterized by two measures of fluorescence emission (chlorophyll and phycoerythrin), its diameter (estimated from light scatter measurements by the application of Mie theory for spherical particles), its carbon content (cell volume is converted to carbon content) and its label (identified based on a combination of manual gating and a semi-supervised clustering method), as described in Ribalet et al. [2019]. Note that we use the particle labels only for comparison to our approach in Section 4.1. Particles were aggregated by hour, resulting in $T = 296$ cytograms for the duration of the cruise, with matching time points as rows of \mathbf{X} .

Lastly, the cytogram data $\{\mathbf{y}_i^{(t)} \in \mathbb{R}^3 : i = 1, \dots, n_t\}_t$ were log transformed due to skewness of the original distributions, augmented with biomass multiplicity $\{C_i^{(t)} : i = 1, \dots, n_t\}_t$, and binned using $D = 40$ equally sized bins in each dimension, as described in Section 2.3. In the analyses to follow in Sections 4.0.1 - 4.0.2, we consider two data representations for analysis: a $d = 1$ case with only the binned cell diameter biomass cytograms, and the full $d = 3$ dimensional binned biomass cytograms.

Practicalities. The regularization parameters $(\lambda_\alpha, \lambda_\beta)$ were chosen using 5-fold cross-validation as described in Section 2.6. Every application of the EM algorithm was repeated 5 times (for 3-dimensional data) or 10 times (for 1-dimensional example). The model means were restricted using a ball constraint of radius r as described in Section 2.2. In the 1-dimensional data analysis in 4.0.1, the radius reflects the underlying assumption that carbon quotas should at most double or halve, peaking during the day due to carbon fixation via photosynthesis by the cell, and halving due to cell division (i.e. the mother cell divides into two equal daughter cells). Assuming spherical particles, this would correspond to a log scale day-night cell diameter difference of $\log(2)/3 \simeq 0.231$, halved to obtain $r = 0.1153$. The 3-dimensional data analysis in Section 4.0.2 first shifts and scales the log cell diameter to be in the same range as the other axes, and uses $r = 0.5$, which is similar in scale to the radius used in the 1-dimensional analysis.

4.0.1 Application to 1-dimensional cell diameter data

In this section, we apply our model to 1-dimensional cytograms at the hourly time resolution. The 1-dimensional setting is useful for visualization because single plots can display the entire data and fitted model parameters, displaying cluster means $\{\boldsymbol{\mu}_k \in \mathbb{R}^T\}_1^K$ as lines and cluster probabilities $\{\pi_k \in \mathbb{R}^T\}_1^K$ as line thickness, as well as shaded approximate 95% conditional density intervals from $\phi(\cdot, \boldsymbol{\mu}_{kt}, \boldsymbol{\Sigma}_k)$. The estimated means and probabilities are shown in Figure 7, and the estimated coefficients can be seen in Table 2 of the Supplement.

Overall, the estimated model effectively captures the visual patterns in the cytogram data. Clusters 3 and 5 correspond to two well-known populations called *Synechococcus* and *Prochlorococcus*, respectively. The most prominent phenomenon is the daily fluctuation of the mean of cluster 5, which is clearly predicted using a combination of time-lagged sunlight and ocean altimetry. Also notable is change in probability of cluster 3, which is predicted well by physical and chemical covariates such as sea surface temperature and phosphate. The overlapping two clusters 3 and 4 are also accurately captured as separate clusters.

As we will see shortly in the 3-dimensional analysis, introducing the other two axes of the cytograms (i.e. 1-dimensional cytograms to 3-dimensional cytograms) clearly helps further distinguish between clusters and identify finer-grain cluster mean movement. Furthermore, cluster 4, which has a large variance and serves as a *catch-all* background cluster, does not appear to represent a specific

cell population, and rather exists to improve the other clusters' model fits.

We also estimated the *stability* of β coefficients of this model, by calculating the nonzero proportion of each of the estimated coefficients produced from subsampled datasets. These nonzero proportions are displayed alongside the original coefficient estimates in Tables 7 and 8 in the Supplement, and the entire procedure is detailed in Supplement D. The stability estimates seem quite sensible – they show high nonzero probability of sunlight variables for *Prochlorococcus* (cluster 5), as well as overall low nonzero probabilities for the covariates of cluster 4, the background cluster.

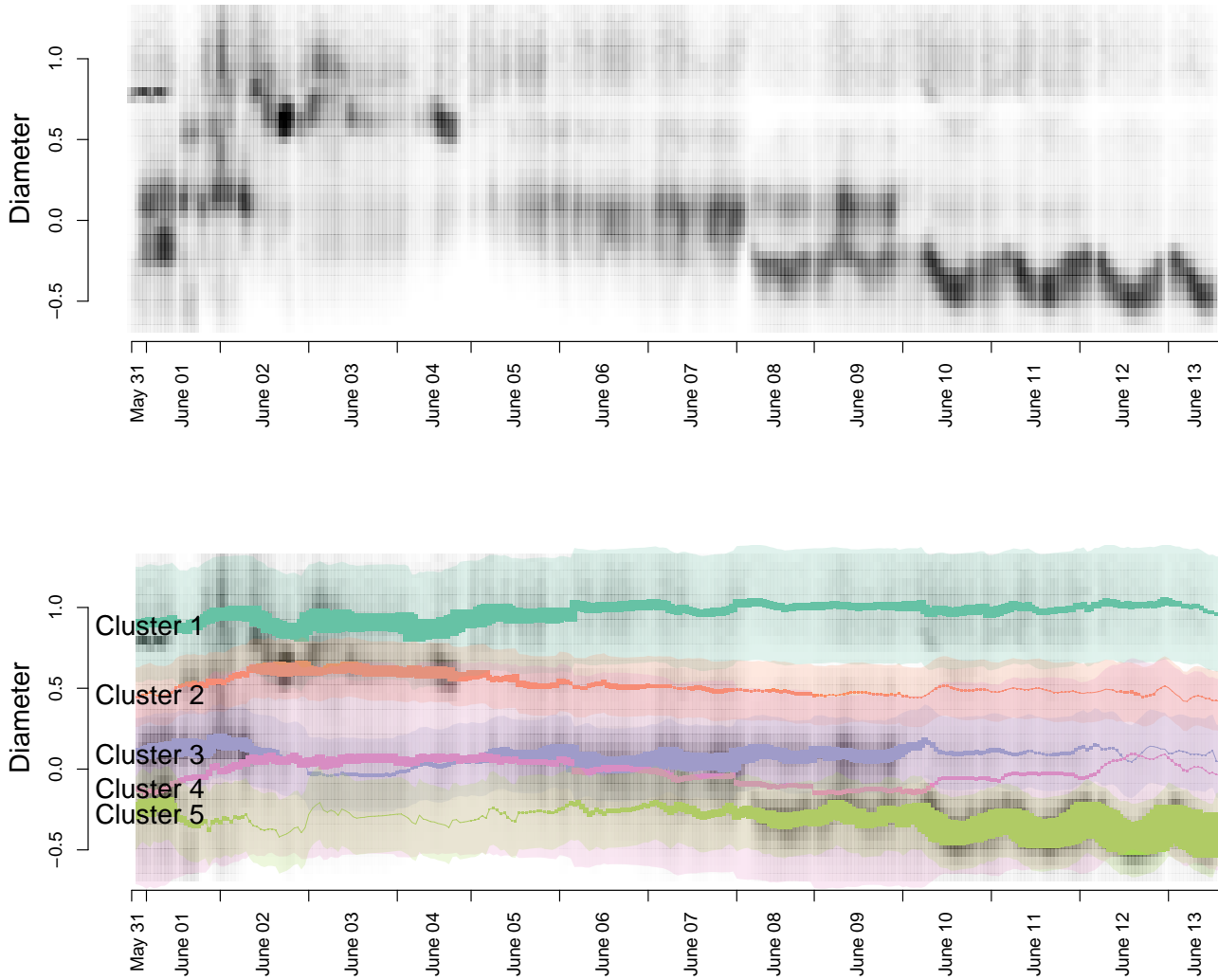


Figure 7: (Top) The 1-dimensional cell diameter biomass cytograms (log transformed) at an hourly time resolution is shown here. In the background, the 1-dimensional biomass distribution of binned cell diameter data is shown in greyscale. (Bottom) The estimated 5-cluster model is overlaid on the same plot; the five solid lines are the five estimated cluster means, whose thickness show the values of the $K = 5$ cluster probabilities $\{\pi_{kt}\}_{k=1}^K$ over time $t = 1, \dots, 296$ (individual hours). The shaded region around the solid lines are the estimated ± 2 standard deviation around the cluster means.

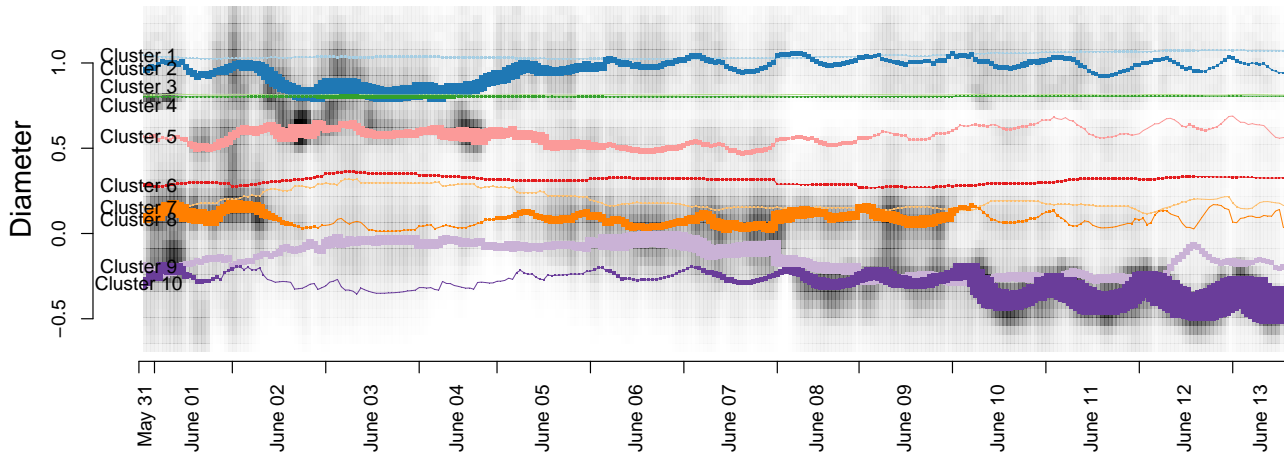


Figure 8: A one-dimensional slice of the estimated model of the full 3-dimensional data, showing only the cell diameter axis. This figure is directly comparable to Figure 7 using only 1-dimensional cell diameter data. The colored solid lines track the ten estimated cluster means over time, and the line thickness shows the cluster probabilities over time. (The shaded 95% probability regions were omitted for clarity of presentation.) This model on 3-dimensional data suggests finer movement of a larger number of cell populations that is not detectable using only the 1-dimensional data. In particular, a clean separation of the heavily overlapping clusters 9 and 10 was not possible in the 1-dimensional model, but is clear in the 3-dimensional model (also see Figure 9 that this separation is made apparent by using the additional *red* axis).

4.0.2 Application to 3-dimensional data

In this section, we apply our model to the full 3-dimensional data. First, in Figure 8, we display one dimension (cell diameter) of the estimated 10-cluster 3-dimensional model, as a direct comparison to the 1-dimensional cell diameter analysis in Section 4.0.1. Cluster 10 is recognized by domain experts to correspond to *Prochlorococcus*. The separation of the two heavily overlapping clusters 9 and 10, and their independent means' movement, are visually not apparent in the cell diameter data alone; indeed, the estimated 1-dimensional model in Figure 7 only captures a single *Prochlorococcus* cluster 5.

The full 3-dimensional data and estimated model are challenging to display in print. A better medium than flat images is a video of $t = 1, \dots, T$ images over time, which we show in <https://youtu.be/jSxgVvT2wr4>. Figure 14 of the Supplement shows one frame from this video (corresponding to one t), which overlays with several plots: three 2-dimensional projections of the cytogram, two different angles of the 3-dimensional cytograms, the cruise location on a map, the covariates over time, and the cluster probabilities at each time and as a time series. The first four panels of this snapshot are shown in Figure 9 in higher resolution. The mean fluctuations and cluster probability dynamics over time are clearly captured in the full video, and are explained next, in the context of covariates.

The estimated mean movement and the β coefficients shown in Tables 4-6 in the Supplement reveal interesting scientific insights. The cell diameter of *Prochlorococcus* seems to be well predicted by sunlight and lagged variants of sunlight. To elaborate, the estimated entries of β_5 corresponding to the covariates p_1 , p_2 and p_3 and the cell diameter axis, were estimated as 0.008, 0.010 and 0.013 –

meaning that the mean cell diameters of *Prochlorococcus* are predicted to increase by these amounts with a unit increase in each covariate value. This supports biochemical intuition about the cell size being directly driven by sunlight. Indeed, important physiological processes of phytoplankton cells, including growth, division, and fluorescence (particularly of the pigment chlorophyll-A), are known to undergo diel variability, i.e. timed with the day-night or light cycle.

Estimated cluster probabilities and the coefficients α shown in Tables 3 are also quite interpretable. A higher positive estimated entry of α_k means that a unit increase of that covariate corresponds to a larger increase of the relative probability of the k 'th cluster. The probability of Cluster 8 (which occupies a region in the orange fluorescence axis that clearly corresponds to the *Synechococcus* population) is associated with primary productivity (coefficient value of 0.19), oxygen (0.46) and nitrate (-0.35). Rapid increases in the abundance and biomass of *Synechococcus* associated with high productivity have previously been observed over narrow regions of the Pacific at the boundary between the Subtropical and Subpolar Gyres [Gradoville et al., 2020]. High productivity in the ocean is often linked to high oxygen saturation, a result of oxygen production during photosynthesis, and low nitrate, as a result of consumption of this nutrient required for *Synechococcus*'s cell growth [Moore et al., 2002]. Linkages to such biochemical factors unique to this specific *Synechococcus* cluster are otherwise difficult to identify, but are clearly identified in our model. In contrast, for cluster 10 (*Prochlorococcus*), the largest α coefficients correspond to sea surface temperature (0.87) and phosphate (-0.94). These results reflect this organism's observed distribution in the Pacific Ocean; namely its Subtropical Gyre, where high surface temperatures and low concentrations of phosphate tend to favor small-celled *Prochlorococcus* leading to higher cluster probabilities. Interestingly, nitrate was not detected by the model as a relevant covariate, which is in good agreement with the physiology of *Prochlorococcus*, which often lack the genes necessary for nitrate assimilation [Berube et al., 2015].

On the other hand, the large positive α coefficients for cluster 2 (*Picoeukaryotes*) associated with phosphate (0.35) reflects its more northerly distribution in the North Pacific Subpolar Gyre, a region of the ocean distinguished by higher surface concentration of nutrients including phosphate which allow for greater growth of these relatively larger phytoplankton.

Finally, cluster 3 is particularly interesting as it captures the calibration beads injected by the instrument as an internal standard. The location of this cluster is much more apparent in the full 3-dimensional representation in Figure 9. This is the only population whose origin and location is known a priori, and thus serves as a negative control, which the model is expected to capture. Indeed, in our estimated 10-cluster 3-dimensional model, this bead is clearly captured as a separate population whose mean movement is minimal over time. Interestingly, 3-dimensional models with fewer than 10 clusters fail to capture the calibration bead as a separate population.

4.1 Comparison to gating

In Figure 10, we compare the relative biomass of *Prochlorococcus*, measured in two ways. The dark grey line shows the relative biomass of *Prochlorococcus*, gated in Ribalet et al. [2019] using flowDensity bioconductor package [Malek et al., 2015], applied semi-automatically to individual 3-dimensional cytograms recorded roughly every 3 minutes, then aggregated to an hourly level. There is a noticeable discrepancy between the two methods on June 8th and 9th. The dark grey line abruptly rises from near 0 to about 0.5, while the purple line follows a gradual increase from June 8th onwards. The reasons for this discrepancy are apparent from visual examination of the gated cytograms. First, the gating results have no continuity or smoothness over time, having been applied to individual cytograms. More importantly, while our model consistently tracks the *Prochlorococcus* cluster as a single ellipsoidal cluster 10, the semi-automatic gating function erroneously includes external particles – many from our model's cluster 9, which domain experts would not consider to be *Prochlorococcus*.

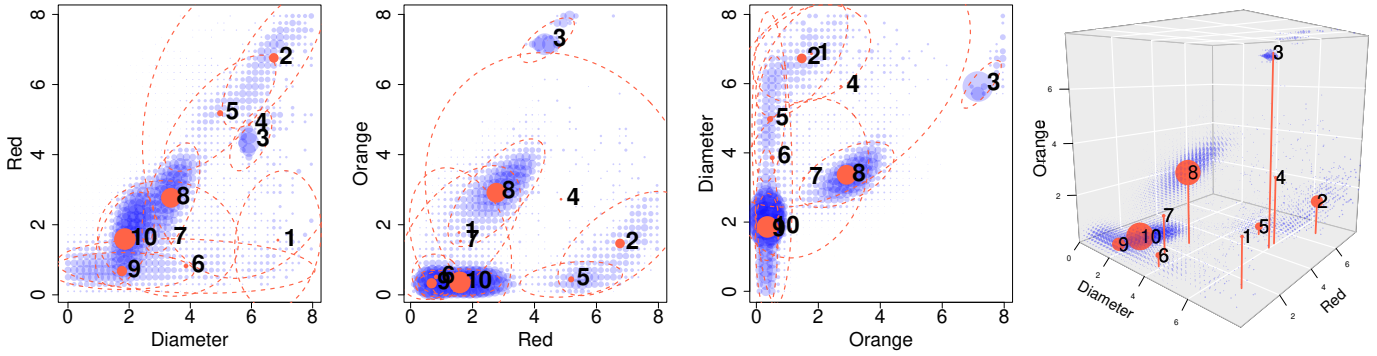


Figure 9: The estimated 3-dimensional 10-cluster model described in Section 4.0.2, at one time point. The size of the blue points represents the biomass in each of the 40^3 bins. The panels show various views of the cytograms – three 2d scatterplots and our estimated parameters (means, probabilities, and covariances). The red dots mark the cluster centers at this time point, and the size (radius) of these red dots are proportional to the cluster probabilities. The red ellipses in dashed lines show the estimated 95% probability region of the data formed from the estimated Gaussian covariance of each cluster. The 10 estimated model clusters’ mean fluctuations and cluster probability dynamics over time can be seen in the full video in <https://youtu.be/jSægVuT2wr4> – a single frame of this video is shown in Figure 9.

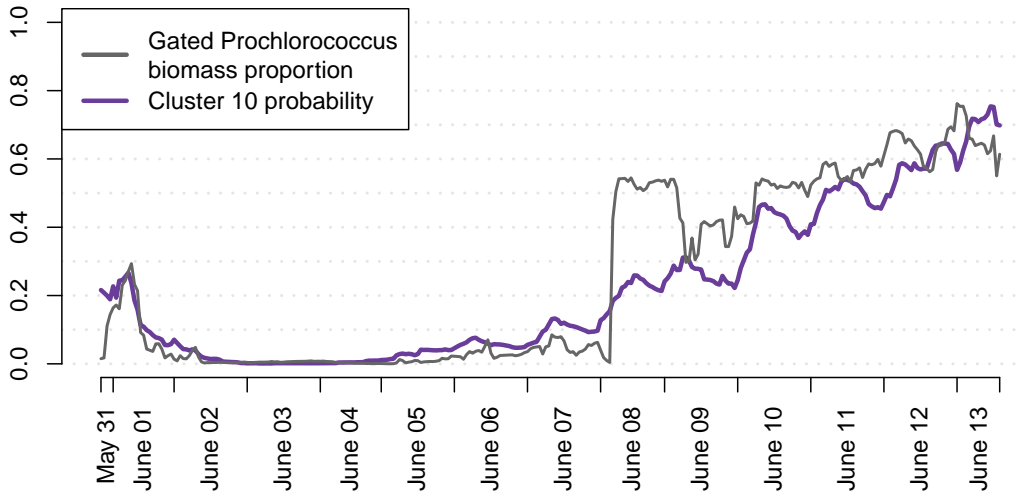


Figure 10: This figure shows the relative biomass of *Prochlorococcus*, measured in two ways – using traditional gating (black line), and using the estimated cluster probability of cluster 10 (purple) in the 3-dimensional data in Section 4.0.2 and Figure 9. One noticeable discrepancy is on June 8th and 9th. The gating (black line) abruptly jumps from 0 to 0.5 due to flaws in automatic gating, while our model (purple) suggests a gradual increase on June 8th and onwards. Visual inspection and expert annotation of this cluster in the cytogram suggests that our model cluster 10 is correctly tracking *Prochlorococcus*.

5 Conclusion

In this work, we propose a novel sparse mixture of multivariate regressions model for modeling flow cytometry data. We devise a penalized expectation-maximization algorithm with parameter constraints and implement a specific ADMM solver, which is called in the M-step. Our simulations and application results in Section 3 and 4 demonstrate that our proposed model can reveal interpretable insights from flow cytometry data, and help scientists identify how environmental conditions influence the dynamics of phytoplankton populations.

Our method provides scientists with a rich description of the association between environmental factors and phytoplankton cell populations. It leverages covariates and all cytograms to identify cell populations. This means two cell populations that might be indistinguishable in a single cytogram could be differentiated if their dynamics (i.e. dependence on covariates) are distinct from each other. Thus, even when one is not interested in the covariates themselves but only the estimation of cell populations (as in gating) this method still may be the best choice. In applying the method, we recover some known associations, such as *Prochlorococcus* and light (positive controls), we did not identify some known non-associations (negative controls), and also produced some new associations that can be studied. Also, in investigating a discrepancy between our method and a pre-existing gating approach, we uncovered some undesirable behavior of the pre-existing approach, and showcased our method’s ability to perform the difficult task of automatic and consistent gating of overlapping clusters in cytograms over time.

While the motivation from this methodology comes from oceanography, the flow cytometry technology is important to many other areas, including biomarker detection [Gedye et al., 2014], diagnosis of human diseases such as tumors [Brown and Wittwer, 2000], and ecological studies [Props et al., 2016]. For instance, in a biomedical application, covariates can be patient attributes, and the response can be cytograms obtained from patient blood samples. In fact, the statistical methodology developed here can be applied to any context in which modeling cytograms in terms of features is reasonable – the time ordering of the data is not required for application. We therefore expect it to be valuable in a wide range of fields.

Our model diagnostics in Supplement E indicate some leftover time dependence in the data residuals from our model. To remedy this within the framework of our model, one might add time-lagged versions of the covariates, or even summaries from cytograms $\mathbf{y}^{(t)}$, to directly incorporate time-space autocorrelation in our model. Alternatively, one could also extend the d -by- d cluster covariance $\Sigma_k \in \mathbb{R}^{d \times d}$ to be a time-varying matrix Σ_{kt} . This covariance matrix can take time structure that is not driven by covariates $X^{(t)}$, but has dependence (e.g. time autocorrelation) or smoothness that is learned directly from the data. However, a time series extension also complicates our existing cross-validation strategy for tuning λ_α and λ_β , and constitutes a significant departure from our current proposed model. We view a time-series extension of our model to be an excellent methodology direction to pursue next.

The methodology has several exciting directions for future work. Our mixture model methodology would greatly benefit from a principled, automatic choice of the number of K based on the data. It would be also be interesting to see how relaxing the Gaussian cluster assumption to different distributions – e.g. skewed, multivariate t distributions – helps improve the flexibility of our approach. A model with feature-dependent covariances $\{\Sigma_k\}_{k=1, \dots, K}$ could enable more flexible prediction as well. Also promising are the extension and comparison to more non-parametric approaches to the conditional distribution of cytograms, or to the entire joint model of cytograms and environmental covariates.

On the application side, it would be interesting to compare estimated models on data from other oceanographic cruises traversing the same trajectory or different areas, and see to what extent the estimated relationship between cytograms and environmental covariates can be replicated.

Acknowledgments

The authors acknowledge the Center for Advanced Research Computing (CARC) at the University of Southern California for providing computing resources that have contributed to the research results reported within this publication. <https://carc.usc.edu>.

This work was supported by grants by the Simons Collaboration on Computational Biogeochemical Modeling of Marine Ecosystems/CBIOMES (Grant ID: 549939 to JB, Microbial Oceanography Project Award ID 574495 to FR). Dr. Jacob Bien was also supported in part by NIH Grant R01GM123993 and NSF CAREER Award DMS-1653017. We thank Dr. E. Virginia Armbrust for supporting SeaFlow deployment on the cruise in the North Pacific funded by the Simons Foundation grant (SCOPE Award ID 426570SP to EVA). We also thank Chris Berthiaume and Dr. Annette Hynes for their help in processing and curating SeaFlow data.

References

- Christopher B. Field, Michael J. Behrenfeld, James T. Randerson, and Paul Falkowski. Primary production of the biosphere: Integrating terrestrial and oceanic components. *Science*, 281(5374): 237–240, 1998. ISSN 0036-8075. doi: 10.1126/science.281.5374.237. URL <https://science.sciencemag.org/content/281/5374/237>.
- Heidi M. Sosik, Robert J. Olson, and E. Virginia Armbrust. Flow Cytometry in Phytoplankton Research. In *Chlorophyll a Fluorescence in Aquatic Sciences: Methods and Applications*, pages 171–185. Springer Netherlands, 2010. doi: 10.1007/978-90-481-9268-7_8.
- George B.J. Dubelaar, Peter L. Gerritzen, Arnout E.R. Beeker, Richard R. Jonker, and Karl Tangen. Design and first results of CytoBuoy: A wireless flow cytometer for in situ analysis of marine and fresh waters. *Cytometry*, 37(4):247–254, Dec 1999. doi: 10.1002/(sici)1097-0320(19991201)37:4(247::aid-cyto1)3.0.co;2-9. URL [https://doi.org/10.1002/\(sici\)1097-0320\(19991201\)37:4<247::aid-cyto1>3.0.co;2-9](https://doi.org/10.1002/(sici)1097-0320(19991201)37:4<247::aid-cyto1>3.0.co;2-9).
- Robert J. Olson, Alexi Shalapyonok, and Heidi M. Sosik. An automated submersible flow cytometer for analyzing pico- and nanophytoplankton: FlowCytobot. *Deep Sea Research Part I: Oceanographic Research Papers*, 50(2):301–315, Feb 2003. doi: 10.1016/s0967-0637(03)00003-7. URL [https://doi.org/10.1016/s0967-0637\(03\)00003-7](https://doi.org/10.1016/s0967-0637(03)00003-7).
- Jarred E Swalwell, Francois Ribalet, and E. Virginia Armbrust. Seaflow: A novel underway flow-cytometer for continuous observations of phytoplankton in the ocean. *Limnology and Oceanography: Methods*, 9(10):466–477, 2011. doi: 10.4319/lom.2011.9.466. URL <https://aslopubs.onlinelibrary.wiley.com/doi/abs/10.4319/lom.2011.9.466>.
- D Vaultot and D Marie. Diel variability of photosynthetic picoplankton in the equatorial Pacific. *Journal of Geophysical Research. C. Oceans*, 104(C2):3297–3310, 1999.
- Heidi M Sosik, Robert J Olson, Michael G Neubert, Alexi Shalapyonok, and Andrew R Solow. Growth Rates of Coastal Phytoplankton from Time-Series Measurements with a Submersible Flow Cytometer. *Limnology and Oceanography*, 48(5):1756–1765, 2003. URL <http://www.jstor.org/stable/3597543>.
- Francois Ribalet, Jarred Swalwell, Sophie Clayton, Valeria Jiménez, Sebastian Sudek, Yajuan Lin, Zackary I. Johnson, Alexandra Z. Worden, and E. Virginia Armbrust. Light-driven synchrony of Prochlorococcus growth and mortality in the subtropical Pacific gyre. *Proceedings of the National Academy of Sciences*, 112(26):8008–8012, jun 2015. ISSN 0027-8424. doi: 10.1073/pnas.1424279112. URL <http://www.pnas.org/lookup/doi/10.1073/pnas.1424279112>.

- Chris P. Verschoor, Alina Lelic, Jonathan L. Bramson, and Dawn M. E. Bowdish. An introduction to automated flow cytometry gating tools and their implementation. *Frontiers in Immunology*, 6(nil):nil, 2015. doi: 10.3389/fimmu.2015.00380. URL <https://doi.org/10.3389/fimmu.2015.00380>.
- Jeremy Hyrkas, Sophie Clayton, Francois Ribalet, Daniel Halperin, E. Virginia Armbrust, and Bill Howe. Scalable clustering algorithms for continuous environmental flow cytometry. *Bioinformatics*, 32(3):417–423, 10 2015. ISSN 1367-4803. doi: 10.1093/bioinformatics/btv594. URL <https://doi.org/10.1093/bioinformatics/btv594>.
- Florian Hahne, Nolwenn LeMeur, Ryan R Brinkman, Byron Ellis, Perry Haaland, Deepayan Sarkar, Josef Spidlen, Errol Strain, and Robert Gentleman. Flowcore: a bioconductor package for high throughput flow cytometry. *BMC Bioinformatics*, 10(1):106, 2009. doi: 10.1186/1471-2105-10-106. URL <https://doi.org/10.1186/1471-2105-10-106>.
- Nima Aghaeepour, Greg Finak, FlowCAP Consortium, DREAM Consortium, Holger Hoos, Tim R Mosmann, Ryan Brinkman, Raphael Gottardo, and Richard H Scheuermann. Critical assessment of automated flow cytometry data analysis techniques. *Nature methods*, 10(3):228–238, March 2013. ISSN 1548-7091. doi: 10.1038/nmeth.2365. URL <https://europepmc.org/articles/PMC3906045>.
- G. J. McLachlan and D. Peel. *Finite Mixture Models*. Wiley, 2006.
- Peiming Wang, Martin L. Puterman, Iain Cockburn, and Nhu Le. Mixed poisson regression models with covariate dependent rates. *Biometrics*, 52(2):381, 1996. doi: 10.2307/2532881. URL <https://doi.org/10.2307/2532881>.
- Abbas Khalili and Jiahua Chen. Variable selection in finite mixture of regression models. *Journal of the American Statistical Association*, 102(479):1025–1038, 2007. doi: 10.1198/016214507000000590. URL <https://doi.org/10.1198/016214507000000590>.
- Nicolas Städler, Peter Bühlmann, and Sara van de Geer. L1-penalization for mixture regression models. *TEST*, 19(2):209–256, 2010. doi: 10.1007/s11749-010-0197-z. URL <https://doi.org/10.1007/s11749-010-0197-z>.
- Bettina Grün and Friedrich Leisch. Flexmix version 2: Finite mixtures with concomitant variables and varying and constant parameters. *Journal of Statistical Software, Articles*, 28(4):1–35, 2008. ISSN 1548-7660. doi: 10.18637/jss.v028.i04. URL <https://www.jstatsoft.org/v028/i04>.
- M.I. Jordan and R.A. Jacobs. Hierarchical mixtures of experts and the em algorithm. In *Proceedings of 1993 International Conference on Neural Networks (IJCNN-93-Nagoya, Japan)*, 1993. doi: 10.1109/ijcnn.1993.716791. URL <https://doi.org/10.1109/ijcnn.1993.716791>.
- Robert Tibshirani. Regression shrinkage and selection via the lasso. *Journal of the Royal Statistical Society. Series B (Methodological)*, 58(1):267–288, 1996. ISSN 00359246. doi: 10.2307/2346178. URL <http://www.jstor.org/stable/2346178>.
- Lei Xu and Michael I. Jordan. On convergence properties of the EM algorithm for gaussian mixtures. *Neural Computation*, 8(1):129–151, jan 1996. doi: 10.1162/neco.1996.8.1.129. URL <https://doi.org/10.1162/neco.1996.8.1.129>.
- Emilio Marañón. Cell Size as a Key Determinant of Phytoplankton Metabolism and Community Structure. *Annual Review of Marine Science*, 7(1):241–264, jan 2015. ISSN 1941-1405. doi: 10.1146/annurev-marine-010814-015955. URL <http://www.annualreviews.org/doi/10.1146/annurev-marine-010814-015955>.

- Wei Pan and Xiaotong Shen. Penalized model-based clustering with application to variable selection. *Journal of Machine Learning Research*, 8:1145–1164, 05 2007.
- Jerome Friedman, Trevor Hastie, and Robert Tibshirani. Regularization paths for generalized linear models via coordinate descent. *Journal of Statistical Software*, 33(1):1–22, 2010. URL <http://www.jstatsoft.org/v33/i01/>.
- Michael Grant and Stephen Boyd. CVX: Matlab software for disciplined convex programming, version 2.1. <http://cvxr.com/cvx>, mar 2014.
- Stephen Boyd, Neal Parikh, Eric Chu, Borja Peleato, and Jonathan Eckstein. Distributed optimization and statistical learning via the alternating direction method of multipliers. *Foundations and Trends® in Machine Learning*, 3(1):1–122, 2011. ISSN 1935-8237. doi: 10.1561/22000000016. URL <http://dx.doi.org/10.1561/22000000016>.
- Timothy P. Boyer, John I. Antonov, Olga K. Baranova, Hernan E. Garcia, Daphne R. Johnson, Alexey V. Mishonov, Todd D. O’Brien, Dan Seidov, Smolyar, I. (Igor), Melissa M. Zweng, Christopher R. Paver, Ricardo A. Locarnini, James R. Reagan, Carla Coleman, and Alexandra Grodsky. World ocean database 2013. *Database*, 2013. doi: 10.7289/V5NZ85MT. URL <https://repository.library.noaa.gov/view/noaa/1291>.
- Mohammad D. Ashkezari, Norland R. Hagen, Michael Denholtz, Andrew Neang, Tansy C. Burns, Rhonda L. Morales, Charlotte P. Lee, Christopher N. Hill, and E. Virginia Armbrust. Simons collaborative marine atlas project (simons cmap): an open-source portal to share, visualize and analyze ocean data. *bioRxiv*, 2021. doi: 10.1101/2021.02.16.431537. URL <https://www.biorxiv.org/content/early/2021/02/17/2021.02.16.431537>.
- Sangwon Hyun, Aditya Mishra, Christian Müller, and Jacob Bien. R package for cmap access, 2020. URL <https://github.com/simonscmap/cmap4r>. [Online; accessed 19-Dec-2019].
- François Ribalet, Chris Berthiaume, Annette Hynes, Jarred Swalwell, Michael Carlson, Sophie Clayton, Gwenn Hennon, Camille Poirier, Eric Shimabukuro, Angelique White, and E. Virginia Armbrust. SeaFlow data v1, high-resolution abundance, size and biomass of small phytoplankton in the north pacific. *Scientific Data*, 6(1), 11 2019. doi: 10.1038/s41597-019-0292-2. URL <https://doi.org/10.1038/s41597-019-0292-2>.
- Mary R. Gradoville, Hanna Farnelid, Angelique E. White, Kendra A. Turk-Kubo, Brittany Stewart, François Ribalet, Sara Ferrón, Paulina Pinedo-Gonzalez, E. Virginia Armbrust, David M. Karl, Seth John, and Jonathan P. Zehr. Latitudinal constraints on the abundance and activity of the cyanobacterium UCYN-A and other marine diazotrophs in the North Pacific. *Limnology and Oceanography*, page lno.11423, mar 2020. doi: 10.1002/lno.11423. URL <https://onlinelibrary.wiley.com/doi/abs/10.1002/lno.11423>.
- Lisa R Moore, Anton F Post, Gabrielle Rocap, and Sallie W Chisholm. Utilization of different nitrogen sources by the marine cyanobacteria *Prochlorococcus* and *Synechococcus*. *Limnology and Oceanography*, 47(4):989–996, 2002. ISSN 00243590. doi: 10.4319/lo.2002.47.4.0989.
- Paul M. Berube, Steven J. Biller, Alyssa G. Kent, Jessie W. Berta-Thompson, Sara E. Roggensack, Kathryn H. Roache-Johnson, Marcia Ackerman, Lisa R. Moore, Joshua D. Meisel, Daniel Sher, Luke R. Thompson, Lisa Campbell, Adam C. Martiny, and Sallie W. Chisholm. Physiology and evolution of nitrate acquisition in *Prochlorococcus*. *The ISME Journal*, 9(5):1195–1207, 2015. ISSN 17517370. doi: 10.1038/ismej.2014.211.
- Mehrnoush Malek, Mohammad Jafar Taghiyar, Lauren Chong, Greg Finak, Raphael Gottardo, and Ryan R Brinkman. flowDensity: reproducing manual gating of flow

cytometry data by automated density-based cell population identification. *Bioinformatics*, 31(4):606–607, feb 2015. ISSN 1367-4803. doi: 10.1093/bioinformatics/btu677. URL <http://www.ncbi.nlm.nih.gov/pubmed/25378466><https://academic.oup.com/bioinformatics/article-lookup/doi/10.1093/bioinformatics/btu677>.

Craig A. Gedye, Ali Hussain, Joshua Paterson, Alannah Smrke, Harleen Saini, Danylo Sirskyj, Keira Pereira, Nazleen Lobo, Jocelyn Stewart, Christopher Go, Jenny Ho, Mauricio Medrano, Elzbieta Hyatt, Julie Yuan, Stevan Lauriault, Maria Kondratyev, Twan van den Beucken, Michael Jewett, Peter Dirks, Cynthia J. Guidos, Jayne Danska, Jean Wang, Bradley Wouters, Benjamin Neel, Robert Rottapel, and Laurie E. Ailles. Cell surface profiling using high-throughput flow cytometry: A platform for biomarker discovery and analysis of cellular heterogeneity. *PLoS ONE*, 9(8):e105602, 8 2014. doi: 10.1371/journal.pone.0105602. URL <https://doi.org/10.1371/journal.pone.0105602>.

Michael Brown and Carl Wittwer. Flow Cytometry: Principles and Clinical Applications in Hematology. *Clinical Chemistry*, 46(8):1221–1229, 08 2000. ISSN 0009-9147. doi: 10.1093/clinchem/46.8.1221. URL <https://doi.org/10.1093/clinchem/46.8.1221>.

Ruben Props, Pieter Monsieurs, Mohamed Mysara, Lieven Clement, and Nico Boon. Measuring the biodiversity of microbial communities by flow cytometry. *Methods in Ecology and Evolution*, 7(11):1376–1385, 7 2016. doi: 10.1111/2041-210x.12607. URL <https://doi.org/10.1111/2041-210x.12607>.

Supplement to “Modeling Cell Populations Measured By Flow Cytometry With Covariates Using Sparse Mixture of Regressions”

Sangwon Hyun^{*1}, Mattias Rolf Cape^{†2}, Francois Ribalet^{‡2}, and Jacob Bien^{§1}

¹*Department of Data Sciences and Operations, University of Southern California*

²*School of Oceanography, University of Washington*

August 5, 2022

Supplement A: Proof of Proposition 1

Proof. Let us denote $\theta := (\alpha, \beta, \Sigma)$ and write $g(\theta)$ in place of $g(\alpha, \beta)$ for brevity. Also recall our shorthand for particles $\mathbf{y} := \{\mathbf{y}_i^{(t)}\}_{i,t}$. First write the penalized likelihood in (3) (and the objective of (7)) as:

$$f(\theta, \mathbf{y}) := -(1/N) \log \mathcal{L}(\alpha, \beta, \Sigma; \{\mathbf{y}_i^{(t)}\}_{i,t}) + g(\theta),$$

to emphasize it is a bivariate function of θ and \mathbf{y} . The latter \mathbf{y} is taken to be a $\mathbb{R}^{d \sum_t n_t}$ vector, having vectorized entries of $\{\mathbf{y}_i^{(t)}\}_{i,t}$. Now, define the particle mapping $h_B : \mathbb{R}^d \rightarrow \mathbb{R}^d$,

$$h_B(\mathbf{y}_i^{(t)}) = \sum_{b=1}^B \tilde{\mathbf{y}}_b \mathbb{1}\{\mathbf{y}_i^{(t)} \in E_b\},$$

which maps a point to the center of the bin containing it. Writing $h_B(\mathbf{y}) = \{h_B(\mathbf{y}_i^{(t)})\}_{i,t}$, we can succinctly express the objective of (6), $f(\theta, h_B(\mathbf{y}))$.

Next, we want to see that $f(\theta, \mathbf{y})$ as a function of \mathbf{y} is Lipschitz over θ i.e. for any datasets \mathbf{y}, \mathbf{y}' in the data domain $\mathbb{R}^{d \sum_t n_t}$, there exists a finite constant L such that,

$$\max_{\theta \in \Theta} |f(\theta, \mathbf{y}) - f(\theta, \mathbf{y}')| \leq L \cdot \|\mathbf{y} - \mathbf{y}'\|_2. \quad (14)$$

By the mean value theorem and Cauchy-Schwarz, there exists $\tilde{\mathbf{y}} \in \mathcal{Y}$ such that:

$$|f(\theta, \mathbf{y}) - f(\theta, \mathbf{y}')| \leq \|\nabla_{\mathbf{y}} f(\theta, \tilde{\mathbf{y}})\|_2 \cdot \|\mathbf{y} - \mathbf{y}'\|_2$$

The gradient of $f(\theta, \mathbf{y})$ has subvectors of the form:

$$\nabla_{\mathbf{y}_i^{(t)}} f(\theta, \mathbf{y}) = \frac{\sum_{k=1}^K \pi_{kt}(\alpha) \cdot \phi(\mathbf{y}_i^{(t)}; \boldsymbol{\mu}_{kt}(\beta), \boldsymbol{\Sigma}_k) \cdot (-1/2) \cdot \boldsymbol{\Sigma}_k^{-1} \cdot (\mathbf{y}_i^{(t)} - \boldsymbol{\mu}_{kt}(\beta))}{\sum_{k=1}^K \pi_{kt}(\alpha) \cdot \phi(\mathbf{y}_i^{(t)}; \boldsymbol{\mu}_{kt}(\beta), \boldsymbol{\Sigma}_k)}.$$

*sangwonh@usc.edu

†mcape@uw.edu

‡ribalet@uw.edu

§jbien@usc.edu

Given that $\Sigma_k \geq c\mathbf{I}_d$ for all k , this is a continuous function on the compact domain $\Theta \times \mathcal{Y}$, so by Weierstrass's extreme value theorem, it attains a finite maximum, and so (14) holds with $L := \max_{(\theta, \mathbf{y}) \in \Theta \times \mathcal{Y}} \|\nabla_{\mathbf{y}} f(\theta, \mathbf{y})\|_2$.

It follows that:

$$\max_{\theta \in \Theta} |f(\theta, h_B(\mathbf{y})) - f(\theta, \mathbf{y})| \leq L \cdot \|h_B(\mathbf{y}) - \mathbf{y}\|_2 \leq L \cdot \sqrt{\sum_{t=1}^T n_t} \cdot R\sqrt{d}B^{-\frac{1}{d}} \xrightarrow{B \rightarrow \infty} 0, \quad (15)$$

using that the largest distance between any $\mathbf{y}_i^{(t)}$ and $h_B(\mathbf{y}_i^{(t)})$, both d -vectors, is smaller than the length $\sqrt{d}RB^{-\frac{1}{d}}$ of the main diagonal of a d -dimensional hypercube. This establishes that $f(\theta, \mathbf{y})$ and $f(\theta, h_B(\mathbf{y}))$ are arbitrarily close *uniformly* in θ , as B increases.

Now, further denote $f(\theta, \mathbf{y})$ as $f(\theta)$, and $f(\theta, h_B(\mathbf{y}))$ as $f_B(\theta)$, whose subscript B emphasizes the dependence on the number of bins B . For any sequence $\tilde{\theta}_B$ of elements taken from the set sequence $\tilde{\Theta}_B$, there exists a convergent subsequence $\tilde{\theta}_{s_B}$ for some sequence s_B , by the Bolzano-Weierstrass theorem. Now, we proceed to show that $\lim_{B \rightarrow \infty} \tilde{\theta}_{s_B}$ is in $\hat{\Theta}$. For any $\hat{\theta} \in \hat{\Theta}$ and $\tilde{\theta}_{s_B}$:

$$f_{s_B}(\tilde{\theta}_{s_B}) \geq f_{s_B}(\hat{\theta}). \quad (16)$$

Taking the lim inf of both sides and using, by (15), that $\lim_{B \rightarrow \infty} f_{s_B}(\hat{\theta}) = f(\hat{\theta})$,

$$\liminf_{B \rightarrow \infty} f_{s_B}(\tilde{\theta}_{s_B}) \geq f(\hat{\theta}). \quad (17)$$

Now, bound $f(\hat{\theta}) - f(\tilde{\theta}_{s_B})$ from above as follows:

$$\begin{aligned} \limsup_{B \rightarrow \infty} [f(\hat{\theta}) - f(\tilde{\theta}_{s_B})] &= \limsup_{B \rightarrow \infty} [f(\hat{\theta}) - f_{s_B}(\tilde{\theta}_{s_B}) + f_{s_B}(\tilde{\theta}_{s_B}) - f(\tilde{\theta}_{s_B})] \\ &\leq 0 + \limsup_{B \rightarrow \infty} [f_{s_B}(\tilde{\theta}_{s_B}) - f(\tilde{\theta}_{s_B})] \quad \text{by (17)} \\ &\leq \limsup_{B \rightarrow \infty} \left[\sup_{\theta} |f_{s_B}(\theta) - f(\theta)| \right] \\ &= 0 \quad \text{by (15)}. \end{aligned}$$

Replacing the lim sup with the limit, we have

$$\lim_{B \rightarrow \infty} f(\tilde{\theta}_{s_B}) = f(\hat{\theta}) \quad (18)$$

Since f is continuous on Θ , we have:

$$\lim_{B \rightarrow \infty} f(\tilde{\theta}_{s_B}) = f(\lim_{B \rightarrow \infty} \tilde{\theta}_{s_B}) = f(\hat{\theta}), \quad (19)$$

which proves the limit $\lim_{B \rightarrow \infty} \tilde{\theta}_{s_B}$ of any convergent subsequence $\tilde{\theta}_{s_B}$ is a minimizer of the function f . This proves our original statement (8). \square

Supplement B: ADMM details

Continuing directly from the end of Section 2.5, we describe the ADMM algorithm for solving (12) in full detail. (As a reminder, the subscript k has been dropped for notational simplicity.) Using augmented variables $\mathbf{U}_Z \in \mathbb{R}^{T \times d}$ and $\mathbf{U}_W \in \mathbb{R}^{p \times d}$ (combined as $\mathbf{U} = \begin{pmatrix} \mathbf{U}_Z \\ \mathbf{U}_W \end{pmatrix} \in \mathbb{R}^{(p+T) \times d}$) and

penalty parameter $\rho \in \mathbb{R}$, the augmented Lagrangian is: ¹

$$L_\rho = \frac{1}{2N} \sum_{i,t} C_i^{(t)} \gamma_{it} (\tilde{\mathbf{y}}_i^{(t)} - \beta^T \tilde{\mathbf{X}}^{(t)})^T \hat{\Sigma}^{-1} (\tilde{\mathbf{y}}_i^{(t)} - \beta^T \tilde{\mathbf{X}}^{(t)}) + \langle \mathbf{U}, (\frac{\mathbf{X}}{\mathbf{I}}) \beta - (\frac{\mathbf{Z}}{\mathbf{W}}) \rangle \quad (20)$$

$$+ \frac{\rho}{2} \| (\frac{\mathbf{X}}{\mathbf{I}}) \beta - (\frac{\mathbf{Z}}{\mathbf{W}}) \|_F^2 + \lambda_\beta \| \mathbf{W} \|_1 + \sum_{t=1}^T \mathbf{1}_\infty (\| \mathbf{Z}^{(t)} \|_2 \leq r).$$

Since L_ρ is a quadratic function of β , we can find the solution by setting the gradient of L_ρ with respect to β^T equal to zero:

$$\nabla_{\beta^T} L_\rho = \frac{1}{N} \sum_{i,t} C_i^{(t)} \gamma_{it} \hat{\Sigma}^{-1} (\beta^T \tilde{\mathbf{X}}^{(t)} - \tilde{\mathbf{y}}_i^{(t)}) \tilde{\mathbf{X}}^{(t)T} + \mathbf{U}^T (\frac{\mathbf{X}}{\mathbf{I}}) + \rho \left[\beta^T (\frac{\mathbf{X}}{\mathbf{I}})^T - (\frac{\mathbf{Z}}{\mathbf{W}})^T \right] (\frac{\mathbf{X}}{\mathbf{I}}) = \mathbf{0}. \quad (21)$$

The first term in (21) can be simplified using $\tilde{\mathbf{y}}^{(t)} := \frac{1}{N} \sum_i C_i^{(t)} \gamma_{it} \tilde{\mathbf{y}}_i^{(t)}$ and $\mathbf{D} := \text{diag}(\{\frac{1}{N} \gamma_t / \sum_t \gamma_t\}_t)$, (recalling that $\gamma_t := \sum_{i=1}^{n_t} C_i^{(t)} \gamma_{it}$.) as follows:

$$\begin{aligned} & \frac{1}{N} \sum_{i,t} C_i^{(t)} \gamma_{it} \hat{\Sigma}^{-1} (\beta^T \tilde{\mathbf{X}}^{(t)} - \tilde{\mathbf{y}}_i^{(t)}) \tilde{\mathbf{X}}^{(t)T} \\ &= \hat{\Sigma}^{-1} \beta^T \sum_t \left(\frac{1}{N} \sum_i C_i^{(t)} \gamma_{it} \right) \tilde{\mathbf{X}}^{(t)} \tilde{\mathbf{X}}^{(t)T} - \hat{\Sigma}^{-1} \sum_t \underbrace{\frac{1}{N} \sum_i C_i^{(t)} \gamma_{it} \tilde{\mathbf{y}}_i^{(t)}}_{\tilde{\mathbf{y}}^{(t)}} \tilde{\mathbf{X}}^{(t)T} \\ &= \hat{\Sigma}^{-1} \beta^T \tilde{\mathbf{X}}^T \underbrace{\mathbf{D}}_{\text{diag}(\{\frac{1}{N} \gamma_t / \sum_t \gamma_t\}_t)} \tilde{\mathbf{X}} - \hat{\Sigma}^{-1} \tilde{\mathbf{y}}^T \tilde{\mathbf{X}}. \end{aligned}$$

Using this, (21) can be rewritten as:

$$\nabla_{\beta^T} L_\rho = \hat{\Sigma}^{-1} \beta^T \tilde{\mathbf{X}}^T \mathbf{D} \tilde{\mathbf{X}} - \hat{\Sigma}^{-1} \tilde{\mathbf{y}}^T \tilde{\mathbf{X}} + \mathbf{U}^T (\frac{\mathbf{X}}{\mathbf{I}}) + \rho \beta^T (\mathbf{X}^T \mathbf{X} + \mathbf{I}) - \rho (\mathbf{Z}^T \mathbf{X} + \mathbf{W}^T) = \mathbf{0}, \quad (22)$$

which can be further simplified to

$$\hat{\Sigma}^{-1} \beta^T \tilde{\mathbf{X}}^T \mathbf{D} \tilde{\mathbf{X}} + \rho \beta^T (\tilde{\mathbf{X}}^T \tilde{\mathbf{X}} + \mathbf{I}) + \mathbf{E} = \mathbf{0},$$

for $\mathbf{E} := -\hat{\Sigma}^{-1} \tilde{\mathbf{y}}^T \tilde{\mathbf{X}} + \mathbf{U}^T (\frac{\mathbf{X}}{\mathbf{I}}) - \rho (\mathbf{Z}^T \mathbf{X} + \mathbf{W}^T)$ and $\tilde{\mathbf{y}}$ whose rows are $\tilde{\mathbf{y}}^{(t)}$. Lastly, if we multiply $(\mathbf{X}^T \mathbf{X} + \mathbf{I})^{-1}$ on the right and $\hat{\Sigma}$ on the left, and take the transpose, we get:

$$(\mathbf{X}^T \mathbf{X} + \mathbf{I})^{-1} \tilde{\mathbf{X}}^T \mathbf{D} \tilde{\mathbf{X}} \beta + \beta \cdot \rho \hat{\Sigma} + (\mathbf{X}^T \mathbf{X} + \mathbf{I})^{-1} \hat{\mathbf{E}}^T \hat{\Sigma} = \mathbf{0}, \quad (23)$$

which is of the form $\mathbf{A} \beta + \beta \mathbf{B} + \mathbf{C} = \mathbf{0}$ for the matrix-valued variable β and square matrices \mathbf{A} and \mathbf{B} . This is the famed Sylvester equation that is typically solved the Bartels-Stewart algorithm [Bartels and Stewart, 1972], an algorithm that is well studied and implemented in major software packages (e.g. C++ Armadillo Sanderson and Curtin [2016]).

However, invoking Bartels-Stewart to solve (23) at every ADMM iteration is unnecessarily expensive, since the algorithm always starts with two Schur decompositions of $\mathbf{A} = \rho \hat{\Sigma}$ and $\mathbf{B} = \tilde{\mathbf{X}}^T \mathbf{D} \tilde{\mathbf{X}} (\mathbf{X}^T \mathbf{X} + \mathbf{I})^{-1}$ that do not need to be repeated (i.e. \mathbf{A} and \mathbf{B} are the same for all ADMM iterations in this EM algorithm iteration).

¹The variables and data are of dimension: $\mathbf{Z}^{(t)} \in \mathbb{R}^d$, $\mathbf{W}, \beta \in \mathbb{R}^{p \times d}$, $\mathbf{X} \in \mathbb{R}^{T \times p}$, $\mathbf{X}^{(t)} \in \mathbb{R}^p$, $\mathbf{Z} \in \mathbb{R}^{T \times d}$.

Instead, if we perform the Schur decompositions once before the first ADMM iteration to obtain $\mathbf{A} = \mathbf{U}_A \mathbf{T}_A \mathbf{U}_A^T$ and $\mathbf{B} = \mathbf{U}_B \mathbf{T}_B \mathbf{U}_B^T$ (producing orthonormal matrices $\mathbf{U}_A, \mathbf{U}_B$ and upper-triangular matrices $\mathbf{T}_A, \mathbf{T}_B$), the equation $\mathbf{A}\boldsymbol{\beta} + \boldsymbol{\beta}\mathbf{B} + \mathbf{C} = \mathbf{0}$ to solve at every subsequent ADMM iteration is much faster to solve, since it can be written as:

$$\mathbf{U}_A \mathbf{T}_A \mathbf{U}_A^T \boldsymbol{\beta} + \boldsymbol{\beta} \mathbf{U}_B \mathbf{T}_B \mathbf{U}_B^T + \mathbf{C} = \mathbf{0}. \quad (24)$$

which is equivalent to:

$$\mathbf{T}_A \left(\mathbf{U}_A^T \boldsymbol{\beta} \mathbf{U}_B \right) + \left(\mathbf{U}_A^T \boldsymbol{\beta} \mathbf{U}_B \right) \mathbf{T}_B + \mathbf{U}_A^T \mathbf{C} \mathbf{U}_B = \mathbf{0}, \quad (25)$$

which is a special case of a Sylvester equation – in the variable $\boldsymbol{\beta}' = \mathbf{U}_A^T \boldsymbol{\beta} \mathbf{U}_B$ – that is extremely fast to solve since the coefficients \mathbf{T}_A and \mathbf{T}_B are triangular matrices. The ADMM iterations are run until a particular convergence check is met, described in the next subsection. In addition, in the `flowmix` R package, we use the approach of Xu et al. [2017] to adaptively change the penalty parameter ρ , which makes the algorithm’s convergence more robust compared to when using a fixed choice of ρ .

Convergence criterion

Following Section 3.3 in Boyd et al. [2011], a convergence criterion is established by limiting the *primal* and *dual residuals* of our problem. This can be derived by first framing our augmented problem in (12) in terms of the canonical ADMM problem (using block matrix notation):

$$\begin{aligned} & \underset{\boldsymbol{\beta}, \mathbf{Z}, \mathbf{W}}{\text{minimize}} && f(\boldsymbol{\beta}) + g(\mathbf{Z}, \mathbf{W}) \\ & \text{subject to} && \mathbf{F}\boldsymbol{\beta} + \mathbf{G} \begin{pmatrix} \mathbf{W} \\ \mathbf{Z} \end{pmatrix} = \begin{pmatrix} \mathbf{0} \\ \mathbf{0} \end{pmatrix} \in \mathbb{R}^{(T+p) \times d} \end{aligned} \quad (26)$$

for matrices \mathbf{F} and \mathbf{G} defined as:

$$\mathbf{F} = \begin{pmatrix} \mathbf{I}_p \\ \mathbf{X} \end{pmatrix}, \mathbf{G} = \begin{pmatrix} -\mathbf{I}_p & \mathbf{0} \\ \mathbf{0} & \mathbf{I}_T \end{pmatrix}, \quad (27)$$

where the left-most column of \mathbf{F} is a single zero vector, and $\mathbf{I}_p \in \mathbb{R}^{p \times p}$ and $\mathbf{I}_T \in \mathbb{R}^{T \times T}$ are identity matrices. Using this notation, the primal and dual residuals are written as \mathbf{r} and \mathbf{s} respectively:

$$\begin{aligned} \mathbf{r} &= \mathbf{F}\boldsymbol{\beta} + \mathbf{G} \begin{pmatrix} \mathbf{W} \\ \mathbf{Z} \end{pmatrix} \in \mathbb{R}^{(p+T) \times d} \\ \mathbf{s} &= \rho \mathbf{F}^T \mathbf{G} \left[\begin{pmatrix} \mathbf{W} \\ \mathbf{Z} \end{pmatrix} - \begin{pmatrix} \mathbf{W}^{\text{prev}} \\ \mathbf{Z}^{\text{prev}} \end{pmatrix} \right] \in \mathbb{R}^{p \times d}, \end{aligned}$$

where the \mathbf{W}^{prev} denotes the value of \mathbf{W} from the previous iteration. Since \mathbf{r} and \mathbf{s} are matrices, we use the Frobenius norm in controlling their entrywise size as the stopping rule. The stopping criterion is then

$$\|\mathbf{r}\|_F \leq \epsilon^{\text{pri}} \quad \text{and} \quad \|\mathbf{s}\|_F \leq \epsilon^{\text{dual}},$$

for a stopping tolerance value

$$\begin{aligned} \epsilon^{\text{pri}} &= \epsilon^{\text{rel}} \max \left\{ \|\mathbf{F}\boldsymbol{\beta}\|_F, \left\| \mathbf{G} \begin{pmatrix} \mathbf{W} \\ \mathbf{Z} \end{pmatrix} \right\|_F \right\}, \\ \epsilon^{\text{dual}} &= \epsilon^{\text{rel}} \left\| \mathbf{F}^T \begin{pmatrix} \mathbf{U}_W \\ \mathbf{U}_Z \end{pmatrix} \right\|_F, \end{aligned}$$

for a relative tolerance threshold value $\epsilon^{\text{rel}} = 10^{-3}$.

Supplement C: Additional data analysis results

This section contains additional figures and tables for the data analysis from Section 4. Here is a summary of the material:

1. Figure 11 and Table 1 show plots of all environmental covariates, and longer names of the covariates.
2. Figure 12 and Figure 13 show more detailed results from the 1d data application in Section 4.0.1.
3. Figure 12 shows a 10 by 10 heatmap of the cross-validation scores from the 2d grid of candidate $(\lambda_\alpha, \lambda_\beta)$ values, and Figure 13 shows the estimated models.
4. The estimated coefficients from the 1-dimensional analysis in Section 4.0.1 are shown as tables in Table 2. Additionally, stability estimates are shown in 7 and 8, whose details are described in Supplement D.
5. The estimated coefficients from the 3-dimensional analysis in Section 4.0.2 are shown in Table 3 through Table 6.
6. A frame of a video showing a complete visualization of the 3-dimensional model in Section 4.0.2 is shown in Figure 14.

Supplement D: Variable Selection Stability

In order to quantify uncertainty of our model estimates, we use the subsampling bootstrap [Politis et al., 1999] to estimate stability of β coefficients of our model estimated on the 1-dimensional data in Figure 7. This closely follows the idea of *stability selection* in Meinshausen and Bühlmann [2010] originally designed for regression. To measure stability, we calculate the nonzero proportion of each of the estimated coefficients (β), from 100 subsampled datasets of size 150 from the original dataset of size $T = 296$. These proportions are displayed alongside the original coefficient estimates in Tables 7 and 8. We describe the entire procedure next.

Recall we are denoting model estimates in the full data, after cross-validation, as $\{\hat{\beta}_k \in \mathbb{R}^p\}_{k=1, \dots, K}$. We are not concerned with the intercept coefficient $\hat{\beta}_{k0}$, so we omit it from the procedure hereon. We take the following steps.

1. For $b = 1, \dots, n_{\text{boot}}$, repeat the following steps:
 - (a) Randomly draw $B = 150$ time indices out of $\{1, \dots, 296\}$, and call this set I_b .
 - (b) Take a subsample of the data $\{\mathbf{y}^{(t)}, \mathbf{X}^{(t)}\}_{t \in I_b}$.
 - (c) On this data, estimate the coefficients $\{\hat{\beta}_k^{b,B}\}_{k=1}^K$, with cross-validation. (The b and B in the superscript emphasize that it is from the b 'th subsampled dataset of size B .)
 - (d) Use the matching procedure in Algorithm 1, to find the optimal cluster permutations $\tilde{\pi}$ to most closely match the original clusters from the full data, i.e. the ones in $\{\hat{\beta}_k\}_{k=1}^K$.
 - (e) Reorder cluster assignments of the subsampled coefficient estimates $\{\hat{\beta}_k^{b,B}\}_{k=1}^K$ by assigning new cluster labels $\{\tilde{\pi}(k)\}_{k=1}^K$ to existing clusters $k = 1, \dots, K$.
2. From all models' coefficient estimates $\{\hat{\beta}_k^{b,B}\}_{b=1}^{n_{\text{boot}}}$, calculate stability estimates for each $k = 1, \dots, K$ as:

$$\frac{1}{n_{\text{boot}}} \sum_{b=1}^{n_{\text{boot}}} \mathbf{1}\{\mathbf{e}_j^T \hat{\beta}_k^{b,B} \neq 0\} \text{ for } j = 1, \dots, p.$$

Covariate Name	Long Name
sss	Sea surface salinity
sst	Sea surface temperature
Fe	Mole concentration of dissolved iron in sea water
PP	Net primary productivity of Carbon per unit volume
Si	Mole concentration of Silicate in sea water
NO3	Mole concentration of Nitrate in sea water
CHL	Mass concentration of Chlorophyll in sea water
PHYC	Mole concentration of Phytoplankton expressed as carbon in sea water
PO4	Mole concentration of Phosphate in sea water
O2	Mole Concentration of dissolved Oxygen in sea water
vgosa	Geostrophic velocity anomalies: meridian component
vgos	Absolute geostrophic velocity: meridian component
sla	Sea level anomaly
ugosa	Geostrophic velocity anomalies: zonal component
ugos	Absolute geostrophic velocity: zonal component
wind_stress	Wind stress
eastward_wind	Eastward wind speed
surface_downward_eastward_stress	Eastward wind stress
wind_speed	Wind speed
surface_downward_northward_stress	Northward wind stress
northward_wind	Northward wind speed
ftle_bw_sla	FTLE backward-in-time using geostrophic velocity anomaly
disp_bw_sla	Displacement backward-in-time using geostrophic velocity anomaly
AOU_WOA_clim	Objectively analyzed climatology for apparent oxygen utilization
density_woa_clim	Objectively analyzed climatology for density
o2sat_woa_clim	Objectively analyzed climatology for percent oxygen saturation
oxygen_woa_clim	Objectively analyzed climatology for dissolved oxygen
salinity_woa_clim	Objectively analyzed climatology for salinity
conductivity_woa_clim	Objectively analyzed climatology for conductivity
nitrate_woa_clim	Objectively analyzed climatology for nitrate
phosphate_woa_clim	Objectively analyzed climatology for phosphate
silicate_woa_clim	Objectively analyzed climatology for silicate
par	Photosynthetically active radiation
p1, p2, p3, p4	3-, 6-, 9-, and 12- hour lagged par.
b1, b2	Indicator variables for ecological regions.

Table 1: *The environmental covariates used in our 1d and 3d analysis in Section 4 were retrieved from the Simon’s CMAP database using a process called “colocalization”, which is to take average of moving time/space boxes. The covariate names, except for those in the last two rows, can be used to query data from the Simons CMAP database. For ease of presentation, in Tables 2 through 6, the short hand of $s\text{d}\text{ns}$ and $s\text{d}\text{es}$ is used for `surface_downward_northward_stress` and `surface_downward_northward_stress`, and the suffixes `_WOA_clim` are omitted.*

We use the subsampling bootstrap because the normal bootstrap uses repeated sampling of time points, which complicates our cross-validation of time points by often having data shared in both the training folds and test fold. The subsampling bootstrap, which does not take repeated time

points, eschews this issue.

Supplement E: Probabilistic gating and residual analysis

First, we describe the procedure of drawing cluster membership of a given particle $\mathbf{y}_i^{(t)}$. This procedure can be thought of as *probabilistic gating* (classification) of particles using our mixture-of-regression model. We make use of the posterior membership probability $\gamma_{itk}(\hat{\alpha}, \hat{\beta}, \hat{\Sigma})$ – responsibilities, defined as in (11) – which can be calculated from the estimated model parameters $(\hat{\alpha}, \hat{\beta}, \hat{\Sigma})$. Then, from each particle $\mathbf{y}_i^{(t)}$, a random draw of particle membership $Z_i^{(t)}$ can be made as follows:

$$Z_i^{(t)} = k \text{ with probability } \gamma_{itk}(\hat{\alpha}, \hat{\beta}, \hat{\Sigma}), \text{ for } k = 1, \dots, K.$$

Given the randomly drawn latent membership $Z_i^{(t)}$ of each $\mathbf{y}_i^{(t)}$, we can calculate the residuals by subtracting from $\mathbf{y}_i^{(t)}$ the assigned cluster’s mean. The set of residuals produced are written as,

$$\{\mathbf{r}_{i,t,k} \in \mathbb{R}^3\}_{i=1, \dots, n_{tk}},$$

where n_{tk} is the number of particles that were classified as cluster k . (Note, the results in the remainder of this section are based on a newly fit 10-cluster 3-dimensional *flowmix* model using binned MGL1704 cruise data with finer bins compared to the model fit in Section 4.0.2, in order to calculate higher-resolution binned residuals.)

Figure 15 shows the binned residuals for one dimension – cell diameter – with separate panel for the ten clusters. The color of each bin represents the total biomass in that bin. From simple visual inspection of this plot, it is unclear if any time dependence persists in the residuals. In order to go beyond visual inspection, we devise an approach to quantitatively measure time-dependency based on Wasserstein distance of sphered residual distributions, presented next.

In particular, we investigate whether the k ’th cluster’s 3-dimensional residuals can be deemed white noise if their distributions F_t over time $t = 1, \dots, T$ do not have time dependence. In our setting, we use *sphered* residuals, and use Wasserstein distance as a distance metric for measuring time dependence.

The residuals $\mathbf{r}_{i,t,k}$ are sphered by left-multiplication with the square-root of the estimated covariance matrix of the k ’th population $\Sigma_k^{-1/2} \in \mathbb{R}^{3 \times 3}$. The sphered residuals are $\tilde{\mathbf{r}}_{i,t,k} = \Sigma_k^{-1/2} \mathbf{r}_{i,t,k}$, whose distribution has been standardized to be close to $\mathcal{N}(0, \mathbf{I}_3)$ for 3-by-3 identity matrix \mathbf{I}_3 . The sphered residuals are comparable in size across clusters, which is important in forming a distance measure that is overall consistent in scale. Several examples of this step are shown in Figure 16.

Next, we operate on the 1-dimensional sphered residuals $\{e_m^T \tilde{\mathbf{r}}_{i,t,k}\}_d$ for each cluster $k \in \{1, \dots, K\}$ and dimension $m \in \{1, 2, 3\}$. From each time point t , we obtained the density estimate of one dimension by fitting a 100-bin one-dimensional histogram $h(e_m^T \tilde{\mathbf{r}}_{i,t,k}) \in \mathbb{R}^{100}$ for each time point t , in 100 fixed bins shared across all time points). Then, we calculated the average of 2-Wasserstein distances between $\{e_m^T \tilde{\mathbf{r}}_{i,t,k} : t = 1, \dots, T-l\}$ and the l -lagged version of it $\{e_m^T \tilde{\mathbf{r}}_{i,t,k} : t = l+1, \dots, T\}$:

$$D_{m,k,l} = \frac{1}{T-l} \sum_{t=1}^{T-l} D_2((h(e_m^T \tilde{\mathbf{r}}_{i,t,k}), h(e_m^T \tilde{\mathbf{r}}_{i,t+l,k}))) \quad (28)$$

where $D_2(\mathbf{a}, \mathbf{b})$ is a Wasserstein’s distance of vector \mathbf{a} and \mathbf{b} . This is a measure of l -lag time dependence since it quantifies the average displacement in the space of data between the (i) original sphered residual distributions and (ii) the *time-lagged* version of them. All values of $D_{m,k,l}$ for each value of dimension m and cluster k are plotted in Figure 17, in which each panel is a line plot over l .

We can see in each panel of Figure 17 that all values of $D_{m,k,l}$ have an increasing trend over l . On the right end of each curve, there is a flat plateau of $\{D_{m,k,l}\}_l$ at larger values of l in each panel

– this is because a large time-lag explicitly breaks any time-dependence and effectively guarantees that the distributions under comparison are unrelated. On the left end of each curve, flatness in $D_{m,k,l}$ indicates l -lagged time-independence for small values of l , while a dip in $D_{m,k,l}$ signifies a nonzero time-dependence. Certain panels of Figure 17 flatness in $D_{m,k,l}$ on the left part of each curve, indicating non-appreciable l -lagged time-dependence for small values of l . On the other hand, certain clusters – especially $k \in \{3, 6, 9, 10\}$ – have especially sharp dips for small l which indicates leftover time dependence in the residuals at short lags.

We suggest two possible explanations for the leftover time dependence: (i) There are missing environmental covariates that affect the cytograms but are not accessible to us; and (ii), using smoothly time-varying covariates directly induces some time dependence in the residuals. Our estimated model supports the latter explanation – these clusters ($k \in \{3, 6, 9, 10\}$) correspond to specific well-known marine phytoplankton populations, and have many nonzero large α and β coefficients predicting their mean and relative abundance. The other clusters – especially $k \in \{4, 5\}$ – are non-specific populations and have the smallest coefficient values out of all clusters.

Supplement F: Effect of binning on estimation

Using a simulation, we quantify how much model estimation accuracy suffers as a result of binning the data. We first generated data according to the model described in Figure 4 twenty times. Then, for each dataset, we binned the data using bin sizes $B \in \{5, 10, 20, 30, 40, 50, 100\}$, to create coarsely to finely binned datasets. We estimated models from each dataset, as well as one model from the original unbinned dataset, and used Algorithm 1 to permute these models’ cluster labels to closely match those of a large external dataset. We then computed the entry-wise L2 estimation error of the estimated coefficients $\hat{\beta}$ and cluster means $\{\boldsymbol{\mu}_{kt}(\hat{\beta})\}_{k,t}$ from the binned data to those from the original data. We then plotted this estimation error over the number of bins B , as shown in Figure 18. The thin red lines show the estimation errors from each of the twenty simulations, and the black line shows the median of those values, at each value of B . We can see that the estimation error plateaus to the minimum at a relatively small value of B , at about $B = 20$.

Algorithm 1 Cluster matching algorithm for two models

- 1: **procedure** MATCH CLUSTERS($(\alpha^1, \beta^1, \boldsymbol{\Sigma}^1), (\alpha^2, \beta^2, \boldsymbol{\Sigma}^2), \{\mathbf{y}_{it}\}_{i,t}$) ▷ Two models, and one dataset.
 - 2: Calculate $\{\gamma_{itk}^1\}_{i,t,k}, \{\gamma_{itk}^2\}_{i,t,k}$ from each model using
$$\gamma_{itk}(\alpha, \beta, \boldsymbol{\Sigma}) = \frac{\phi(\mathbf{y}_i^{(t)}; \boldsymbol{\mu}_{kt}(\beta), \boldsymbol{\Sigma}_k) \cdot \pi_{kt}(\alpha)}{\sum_{l=1}^L \phi(\mathbf{y}_i^{(t)}; \boldsymbol{\mu}_{lt}(\beta), \boldsymbol{\Sigma}_l) \cdot \pi_{lt}(\alpha)},$$
 - 3: Form $\boldsymbol{\Gamma}^1, \boldsymbol{\Gamma}^2 \in \mathbb{R}^{(\sum_{t=1}^T n_t) \times K}$ whose rows are $\gamma_{it\cdot}^1 \in \mathbb{R}^K$ and $\gamma_{it\cdot}^2 \in \mathbb{R}^K$,
 - 4: for $i = 1, \dots, n_t$, and $t = 1, \dots, T$.
 - 5: Denote Π as the set of all permutation maps of K elements ▷ Note that $|\Pi| = K!$.
 - 6: $\pi : \{1, \dots, K\} \rightarrow \{1, \dots, K\}$.
 - 7: Denote permutation matrix \mathbf{P}_π of the map π .
 - 8: Calculate $\tilde{\pi} = \operatorname{argmax}_{\pi \in \Pi} KL(\boldsymbol{\Gamma}^1 \mathbf{P}_\pi, \boldsymbol{\Gamma}^2)$.
 - 9: $\triangleright KL(\mathbf{P}_1, \mathbf{P}_2) := \sum_{i,j} \mathbf{Q}_{i,j}$ where $\mathbf{Q} = \mathbf{P}_1 \log(\mathbf{P}_1/\mathbf{P}_2)$ is calculated entrywise for probability matrices $\mathbf{P}_1, \mathbf{P}_2$.
 - 10: **return** $\{\tilde{\pi}(k)\}_{k=1, \dots, K}$ as the cluster labels of model 1 closest to model 2 clusters $1, \dots, K$.
-

Supplement G: Model performance with non-Gaussian data

In order to investigate the model performance when data deviate from mixtures of Gaussians, we consider two such scenarios in a simulation study. The first is when the within-cluster data are more heavy-tailed than Gaussian and the other is when the data are more skewed. In the data setup described in Figure 4 and Section 3.1.1 (with $\sigma_{\text{add}} = 0$ since we are not concerned about covariate noise here) we replace the $\mathcal{N}(0, 1)$ distribution for generating data in each cluster at each time point, with either a t-distribution or a skewed-Normal distribution. These two replacements are described in detail next.

1. **Heavy tails.** The $\mathcal{N}(0, 1)$ is replaced with a t-distribution with degrees of freedom $\nu \in \{3, 5, 10, 20, 40, 100\}$, further divided by $\sqrt{\nu/(\nu - 2)}$ so that the variance is 1, the same as the original distribution.
2. **Skew-normal.** The $\mathcal{N}(0, 1)$ is replaced with a skew-Normal distribution [Azzalini, 2013]. The probability density function of a skew-Normal random variable $X \sim SN(\alpha, \omega, \xi)$ with shape, scale and location parameters α, ω and ξ is:

$$\frac{2}{\omega\sqrt{2\pi}} e^{-\frac{(x-\xi)^2}{2\omega^2}} \int_{-\infty}^{\alpha\left(\frac{x-\xi}{\omega}\right)} \frac{1}{\sqrt{2\pi}} e^{-\frac{t^2}{2}} dt.$$

For a given choice of α , in order to scale and center Z to have mean 0 and variance 1, we further use $\omega(\alpha) = \sqrt{\frac{1}{1-2/\pi} \frac{\alpha^2}{1+\alpha^2}}$ as the scale parameter, and also shift the distribution by $\omega(\alpha) \cdot (\alpha/\sqrt{1+\alpha^2}) \cdot \sqrt{2/\pi}$. The values of α we consider are $\{0, 0.5, \dots, 2\}$.

The simulations from the two setups show that the estimated β model coefficients and cluster means predictably become less accurate as the tails become heavier and the skewness increases (see left and middle panels of Figure 19).

On the other hand, we see some encouraging robustness in variable selection. For each setup – shown in the rightmost panels of Figure 19 – we measured the probability of certain covariates being estimated to be nonzero, averaged across simulations. Recall from the description in Section 3.1.1 that the sunlight covariate is solely responsible for mean movement in both clusters. The nonzero probability of the sunlight covariate remains high and close to 1 even for extremely heavy-tailed data. The changepoint covariates and the eight spurious covariates – which play no role in generating the cluster mean movement – have nonzero probabilities which are initially low but increase as the tails get heavier. With extremely heavy tails – degrees of freedom equal to 3 or 5 – the nonzero probability of the changepoint covariate grows to close to 1, and the nonzero probability of the sunlight covariate decreases slightly, showing that the estimated model tends to erroneously predict cluster mean movement to be piece-wise constant instead of being driven by sunlight.

References

- R. H. Bartels and G. W. Stewart. Solution of the matrix equation $AX + XB = c$ [f4]. *Communications of the ACM*, 15(9):820–826, 9 1972. doi: 10.1145/361573.361582. URL <https://doi.org/10.1145/361573.361582>.
- Conrad Sanderson and Ryan Curtin. Armadillo: a template-based c++ library for linear algebra. *The Journal of Open Source Software*, 1(2):26, 6 2016. doi: 10.21105/joss.00026. URL <https://doi.org/10.21105/joss.00026>.
- Yi Xu, Mingrui Liu, Qihang Lin, and Tianbao Yang. Admm without a fixed penalty parameter: Faster convergence with new adaptive penalization. In I. Guyon, U. Von Luxburg, S. Bengio,

H. Wallach, R. Fergus, S. Vishwanathan, and R. Garnett, editors, *Advances in Neural Information Processing Systems*, volume 30. Curran Associates, Inc., 2017. URL <https://proceedings.neurips.cc/paper/2017/file/e97ee2054defb209c35fe4dc94599061-Paper.pdf>.

Stephen Boyd, Neal Parikh, Eric Chu, Borja Peleato, and Jonathan Eckstein. Distributed optimization and statistical learning via the alternating direction method of multipliers. *Foundations and Trends® in Machine Learning*, 3(1):1–122, 2011. ISSN 1935-8237. doi: 10.1561/22000000016. URL <http://dx.doi.org/10.1561/22000000016>.

Dimitris N. Politis, Joseph P. Romano, and Michael Wolf. *Subsampling*. Springer New York, 1999.

Nicolai Meinshausen and Peter Bühlmann. Stability selection. *Journal of the Royal Statistical Society: Series B (Statistical Methodology)*, 72(4):417–473, 2010.

Adelchi Azzalini. *The Skew-Normal and Related Families*. Institute of Mathematical Statistics Monographs. Cambridge University Press, 2013. doi: 10.1017/CBO9781139248891.

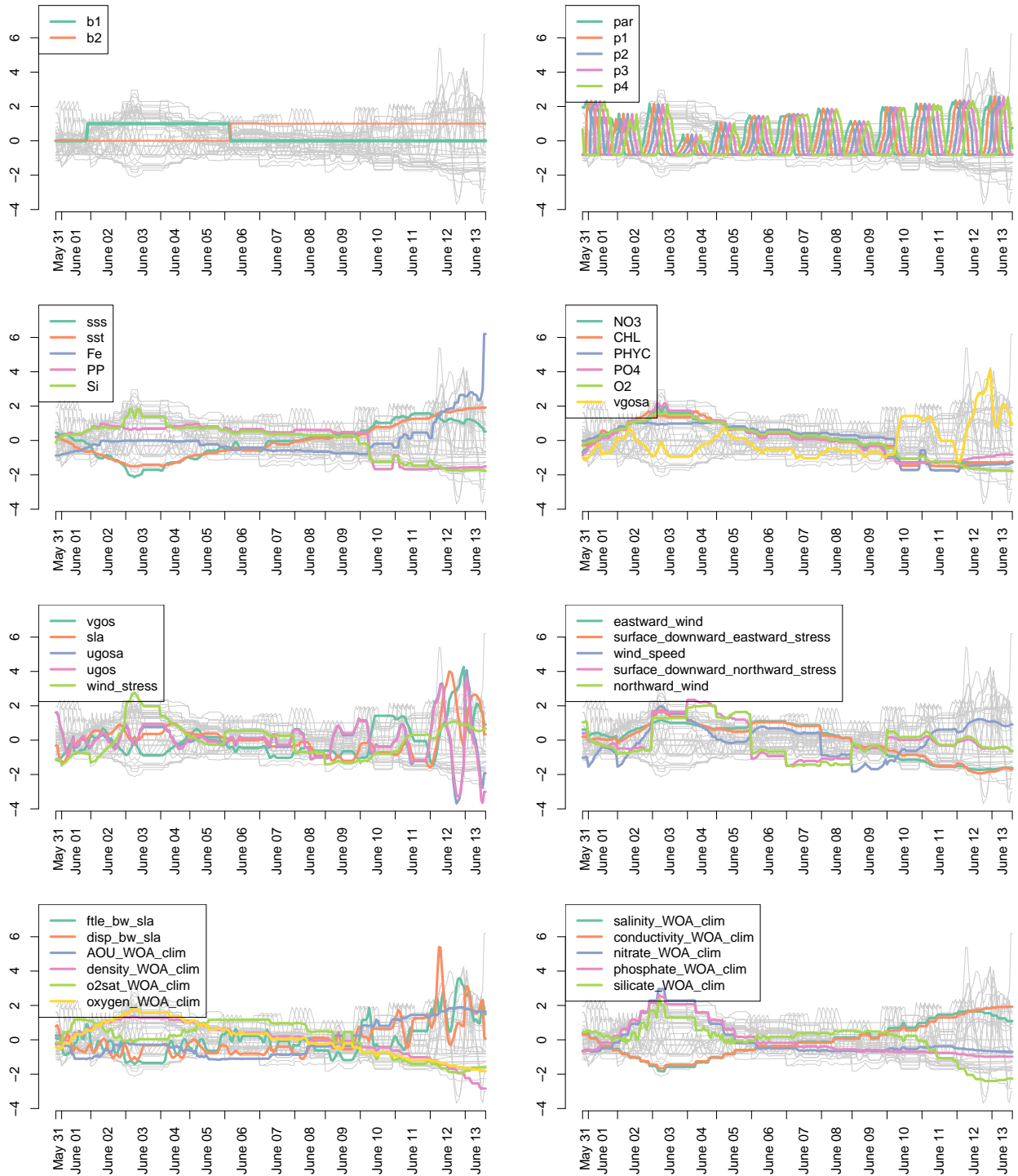


Figure 11: *Eight panels showing the four or five environmental covariates at a time. The first two figures show manually created covariates. In the first figure, b_1 and b_2 are indicator variables for regions crossings of the cruise across an important ecological transition zone. In the second figure, p_1 , p_2 , p_3 , p_4 are the sunlight variable par lagged by 3,6,9 and 12 hours. The rest of the covariates are described briefly in Table 1. All covariates except for b_1 and b_2 were standardized to have mean 0 and sample standard deviation 1.*

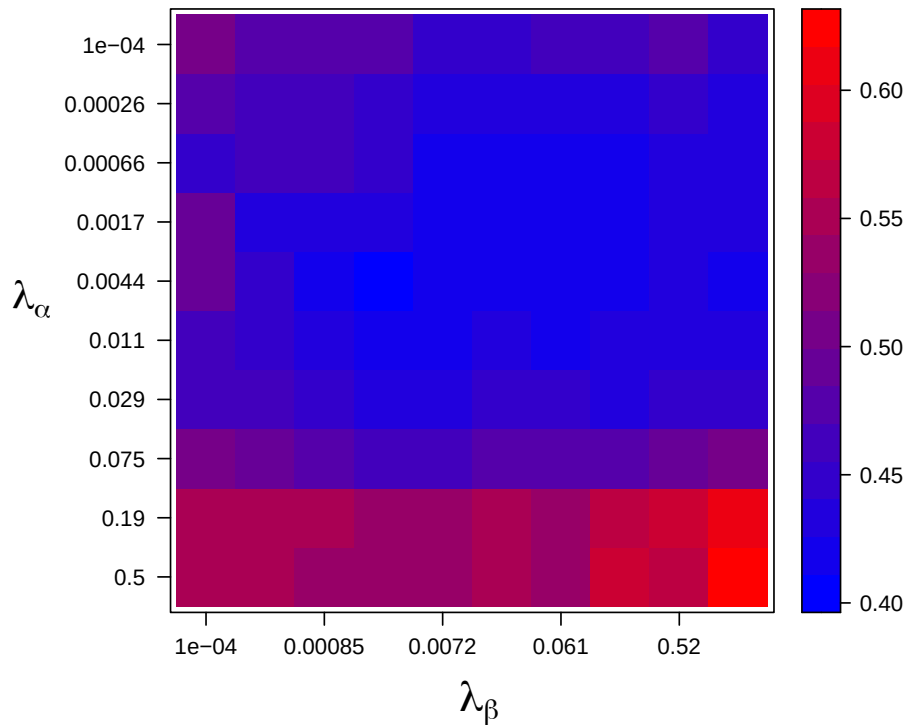


Figure 12: A 10×10 cross-validation (CV) score matrix from the 1-dimensional data analysis in Figure 7 visualized as a 2-dimensional heatmap. Blue shows a low average out-of-sample negative log likelihood across the five CV folds, and red shows high. In this case, the couplet at row 5 and column 4, $\lambda_\alpha = 0.0044$ and $\lambda_\beta = 0.0025$ was chosen. (To be clear, smaller CV score (blue) means a better model according to averaged out-of-sample prediction performance, measured by the negative log-likelihood.)

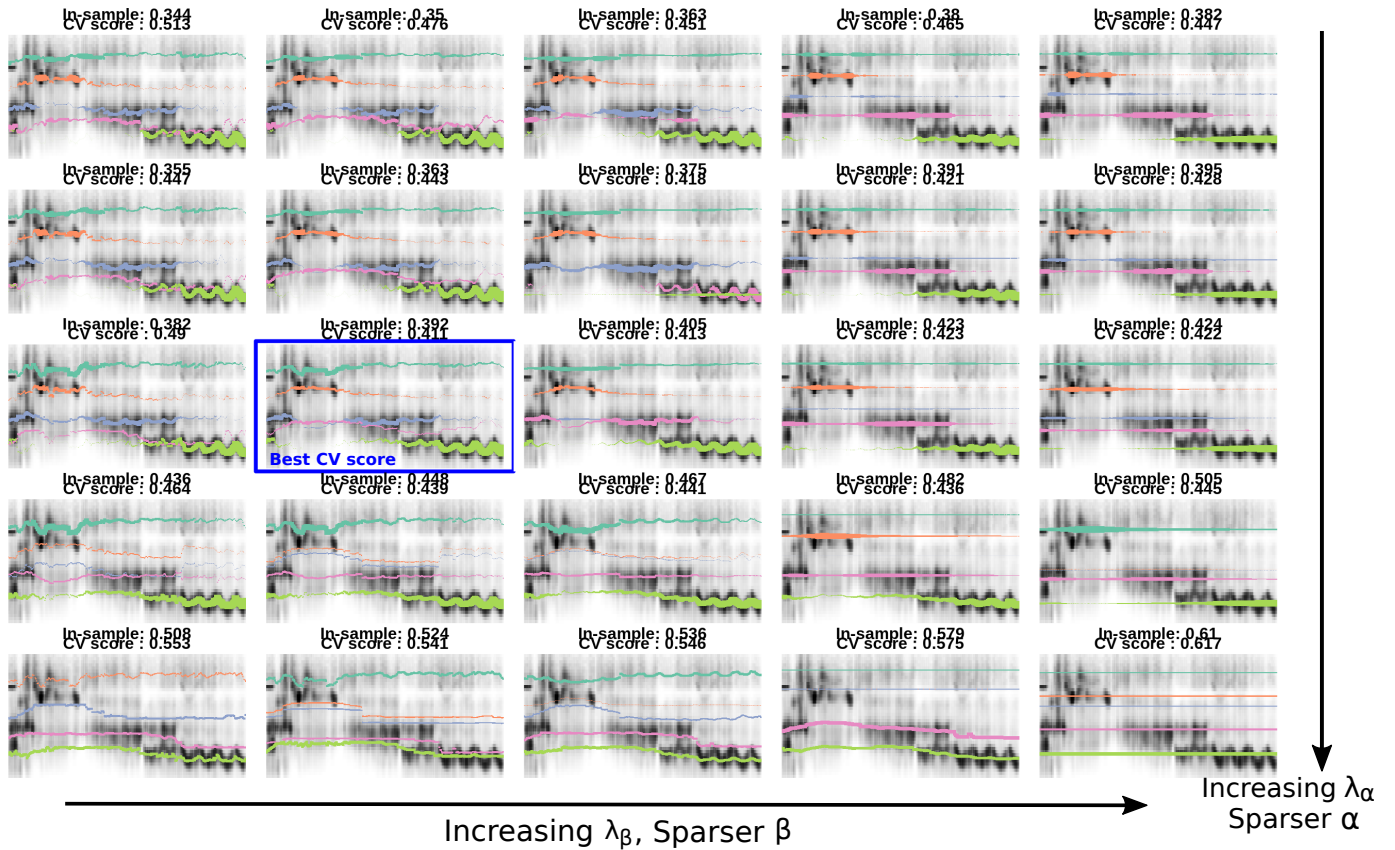


Figure 13: This figure shows $25 = 5 \times 5$ models each from different pairs of $(\lambda_\alpha, \lambda_\beta)$ values, from the 1-dimensional data analysis in Figure 7. The top row shows the models with the lowest λ_α in each column, and the left-most column in each row shows the model with the lowest λ_β value in each row. The top-left figure shows the most complex, least regularized model with all non-zero coefficients – overfitting to the data – and the bottom right shows the simplest, most regularized model with every clusters’ mean and probability constant over time. The blue box highlights the final estimated model with best cross-validated out-of-sample likelihood, as shown in Figure 7. The plot titles show two measures – in-sample objective value, and the average out-of-sample negative log-likelihood across 5 cross-validation test folds; these show that the complex models perform well in-sample, but the cross-validation score suggests the best model is in the middle. The actual cross validation for the analysis was done using a 10×10 2d grid of $(\lambda_\alpha, \lambda_\beta)$ values, but this plot only shows a subset of the rows and columns, for illustration purposes. Figure 12 shows the full 10×10 cross-validation score matrix, visualized as a heatmap.

Covariate name	type	Cluster 1	Cluster 2	Cluster 3	Cluster 4	Cluster 5
p2	light	.	-0.231	-0.005	.	0.006
p3	light	.	-0.007	.	.	.
par	light	0.018	.	.	.	-0.027
sst	phys	0.913
vgosa	phys	.	.	-0.116	.	.
vgos	phys	0.133
sla	phys	.	0.185	.	.	.
ugos	phys	.	-0.134	0.022	.	-0.086
wind_stress	phys	.	.	.	0.011	.
wind_speed	phys	-0.165
northward_wind	phys	0.138	.	.	.	-0.063
f1le_bw_sla	phys	0.032	.	-0.094	.	.
disp_bw_sla	phys	0.018
PP	bio	.	.	0.088	.	.
CHL	bio	.	0.134	.	.	-0.045
o2sat	bio	.	.	0.280	.	.
nitrate	chem	.	.	-0.636	.	.
phosphate	chem	.	0.158	.	.	-0.860
silicate	chem	-0.015

Covariate name	type	Cluster 1	Cluster 2	Cluster 3	Cluster 4	Cluster 5
p1	light	0.002	0.004	0.000	-0.002	0.008
p2	light	.	-0.004	0.006	-0.006	0.013
p3	light	0.007	.	0.005	-0.004	0.010
p4	light	-0.004	0.010	0.002	-0.002	-0.006
par	light	0.002	.	0.004	-0.002	0.002
sst	phys	.	-0.028	-0.004	.	-0.070
vgosa	phys	.	0.014	.	0.025	.
vgos	phys	0.012	.	.	.	-0.006
sla	phys	0.004	-0.012	0.001	0.002	-0.022
ugosa	phys	.	.	-0.005	0.007	-0.050
ugos	phys	0.005	0.007	.	.	0.059
wind_stress	phys	0.011	.	-0.029	.	0.025
eastward_wind	phys	-0.023	.	-0.020	.	0.021
sdes	phys	.	.	-0.011	.	.
wind_speed	phys	.	.	.	0.033	.
sdns	phys	.	-0.002	.	-0.007	0.011
northward_wind	phys	.	-0.009	-0.008	.	.
f1le_bw_sla	phys	0.005	.	0.025	0.000	-0.011
disp_bw_sla	phys	0.001	.	0.004	.	-0.003
density	phys	.	0.026	.	0.051	-0.038
PP	bio	0.066	.	-0.008	.	.
CHL	bio	-0.141
o2sat	bio	0.010	-0.004	0.017	.	-0.022
Si	chem	0.014	-0.021	.	.	-0.005
phosphate	chem	.	0.052	.	0.012	-0.132
silicate	chem	-0.016	-0.022	.	-0.045	-0.001

Table 2: *Estimated α coefficients (top) β coefficients (bottom) for the 5-cluster, 1-dimensional model in Figure 7. Some of the names of the covariates are abbreviated from the full versions in Table 1. The rows (covariates) whose coefficients were all estimated to be zero were omitted. Additionally, stability estimates for the β coefficients are shown in Tables 7 and 8.*

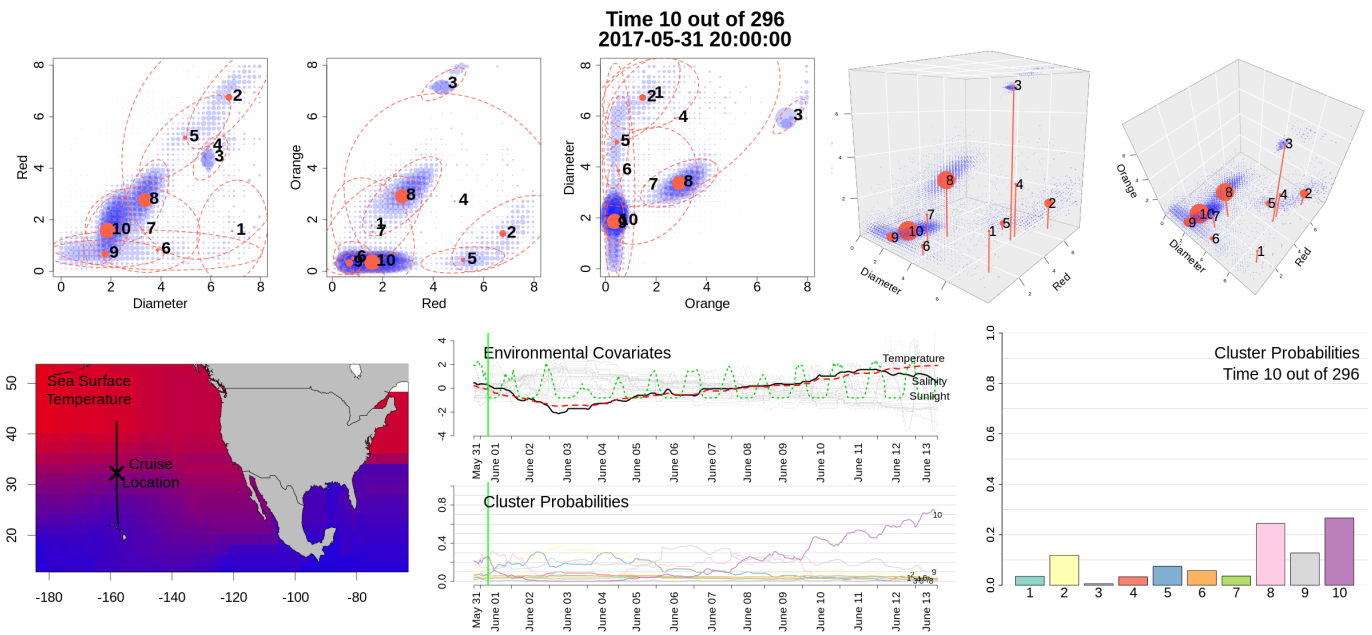


Figure 14: A frame of a video (<https://youtu.be/jSægVuT2wr4>) showing the estimated 3-dimensional 10-cluster model described in Section 4.0.2 and Figure 9. The size of the blue points represents the biomass in each of the 40^3 bins. The top panel shows various views of the cytograms and our estimated parameters (means, probabilities, and covariances). The lower panel shows the cruise location on a map, covariates over time, and finally cluster probabilities at each time and as a time series. The 10 estimated model clusters' mean fluctuations and cluster probability dynamics over time can be seen in the full video.

Covariate	type	Cluster 1	Cluster 2	Cluster 3	Cluster 4	Cluster 5	Cluster 6	Cluster 7	Cluster 8	Cluster 9	Cluster 10
p1	light	.	.	0.086	0.012	.
p2	light	-0.130	0.058
p3	light	0.047	-0.038	0.018
p4	light	-0.023	.
par	light	.	.	0.431	0.013	-0.079
sst	phys	0.868
vgosa	phys	-0.061	.
vgos	phys	.	0.079	-0.002	-0.088	.	.
sla	phys	.	.	.	0.025	0.201	.	.	-0.056	.	.
ugosa	phys	.	0.025	-0.034
ugos	phys	-0.188	.	.	0.175	.	-0.060
wind_stress	phys	0.160	.	-0.436	0.036	-0.085	.	.	-0.371	0.108	.
sdes	phys	0.140	.
wind_speed	phys	-0.255
northward_wind	phys	0.019	-0.181	.	-0.105
f1le_bw_sla	phys	-0.180	.	.
disp_bw_sla	phys	-0.161	0.011
density	phys	.	0.111	.	.	0.429
pp	bio	0.195	.	.
chl	bio	0.214	-0.061
o2sat	bio	-0.143	-0.049	.	0.455	0.003	.
AOU	chem	-0.020	0.032
nitrate	chem	0.015	.	.	0.298	.	.	.	-0.347	-0.005	.
phosphate	chem	.	0.348	-0.937

Table 3: Estimated α coefficients for 10-cluster, 3-dimensional model from Section 3. Rows whose coefficients are all zero have been omitted.

Covariate name	Covariate type	Clust 1		Clust 2		Clust 3		Clust 4	
		Diam	Red	Diam	Red	Diam	Red	Diam	Red
p1	light	.	.	0.031	.	.	0.088	-0.000	.
p2	light	.	.	0.044	-0.004	0.003	.	.	.
p3	light	.	.	0.042	.	0.002	0.005	.	.
p4	light	.	.	0.009	.	.	-0.012	.	.
par	light	.	-0.015	0.040	-0.015
sst	phys	0.011
vgosa	phys	.	.	0.004
vgos	phys	.	.	0.060
sla	phys	.	.	.	-0.040	.	-0.002	.	0.048
ugosa	phys	-0.044	.	.
ugos	phys	.	.	0.014
wind_stress	phys	.	.	.	0.002	0.004	.	.	.
eastward_wind	phys	-0.010	.	.	.	0.068	.	.	.
sdes	phys	.	.	.	0.014
wind_speed	phys	.	.	-0.022	0.024
sdns	phys
northward_wind	phys	.	.	0.031	-0.019
ftle_bw_sla	phys	.	.	0.004
disp_bw_sla	phys	0.003	-0.015	0.007
density	phys
pp	bio	.	.	0.270	-0.053	0.023	.	.	.
chl	bio	.	.	-0.393
o2sat	bio	-0.047	0.015	0.118	0.137	.	.	-0.005	.
si	chem	.	.	.	0.030
AOU	chem
nitrate	chem	.	.	-0.009	.	-0.051	.	.	.
phosphate	chem
silicate	chem	.	0.023	-0.032	0.009	-0.018	.	.	-0.016

Table 4: Estimated β coefficients from the 10-cluster, 3-dimensional model in Section 3. (part 1 of 3). The column names Diam, Red and Orange refer to the names of the 3-dimensional cytogram axes.

Covariate name	Covariate type	Clust 5 Diam	Clust 5 Red	Clust 5 Orange	Clust 6 Diam	Clust 6 Red	Clust 6 Orange	Clust 7 Diam	Clust 7 Red	Clust 7 Orange	Clust 8 Diam	Clust 8 Red	Clust 8 Orange
p1	light	.	-0.004	.	.	.	-0.005	.	.	.	0.029	-0.016	.
p2	light	0.042	-0.002	-0.002	.	.	-0.000	-0.028	.	.	0.034	-0.005	0.018
p3	light	0.036	0.035	-0.006	.	.	-0.005	.	.	.	0.040	0.022	.
p4	light	.	0.065	-0.003	.	.	-0.005	0.018	0.025
par	light	0.035	-0.016	0.001	.	.	-0.002	.	.	.	0.020	.	0.039
sst	phys	-0.001
vgosa	phys	0.094	.	0.011	.	.	.	0.071	.	.	.	-0.020	.
vgos	phys	0.044	.	.
sla	phys	0.002	.	.	0.049	-0.011	0.014
ugosa	phys	0.040	.	0.005	.	-0.006
ugos	phys	.	0.014	-0.074	.	0.063
wind_stress	phys	.	-0.062	-0.096	-0.056
eastward_wind	phys	.	.	0.018	.	0.044	.	.	0.044	.	-0.016	.	.
sdes	phys	0.016	-0.051	.
wind_speed	phys	-0.092	.	0.010	0.090	-0.112	0.078	0.097
sdns	phys	0.002	-0.073	0.022	.	.
northward_wind	phys	-0.001	.	0.025	.	.	.	0.015	-0.002
ftle_bw_sla	phys	.	0.056	0.099	0.075	0.006
disp_bw_sla	phys	0.066	.	-0.015
density	phys	0.046	0.020
pp	bio	.	-0.396	.	.	.	0.007	-0.114	-0.099
chl	bio	.	0.215	0.039	-0.137	0.185	0.081
o2sat	bio	-0.175	.	-0.028	0.002	0.135	.
si	chem	0.266	.	.
AOU	chem	-0.168
nitrate	chem	.	0.049	.	.	.	0.045	0.005	.	.	.	-0.017	.
phosphate	chem	0.128	0.096	0.028	0.013	.	.	0.197	0.042
silicate	chem	.	0.095	-0.002	-0.101

Table 5: Estimated β coefficients from the 10-cluster, 3-dimensional model in Section 3. (part 2 of 3). The column names Diam, Red and Orange refer to the names of the 3-dimensional cytogram axes.

Covariate name	Covariate type	Clust 9 Diam	Clust 9 Red	Clust 9 Orange	Clust 10 Diam	Clust 10 Red	Clust 10 Orange
p1	light	-0.017	0.012	-0.002	0.040	-0.020	0.001
p2	light	-0.008	0.000	-0.001	0.073	0.013	.
p3	light	-0.026	.	-0.003	0.022	-0.028	-3.659e-05
p4	light	-0.006	.	-0.000	-0.003	.	.
par	light	.	0.001	-0.000	0.024	-0.059	.
sst	phys	.	-0.036	.	-0.315	.	.
vgosa	phys	0.061	.	.	.	-0.024	.
vgos	phys	.	0.002	0.002	-0.020	.	-0.000
sla	phys	0.074	-0.002	.	-0.028	-0.014	.
ugosa	phys	.	.	0.003	-0.046	-0.016	0.000
ugos	phys	0.034	.	.	0.057	.	.
wind_stress	phys	.	-0.032	.	-0.018	.	.
eastward_wind	phys	0.114	0.010	0.011	.	0.048	0.012
sdes	phys	0.139	.	.	-0.029	-0.083	.
wind_speed	phys	0.136	0.043	0.005	.	0.003	0.007
sdns	phys	0.006	.	0.004	.	.	.
northward_wind	phys	.	-0.012	.	0.001	.	.
ftle_bw_sla	phys	.	.	0.002	0.003	-0.021	.
disp_bw_sla	phys	-0.056	.	.	-0.018	-0.008	-0.001
density	phys	0.031	.	.	-0.060	0.020	.
PP	bio	.	-0.016	.	0.077	.	.
CHL	bio	.	.	0.001	.	0.098	.
o2sat	bio	0.038	0.025	-0.000	-0.041	.	.
Si	chem	-0.010	.	-0.002	.	0.014	.
AOU	chem	-0.029	.
nitrate	chem	.	.	.	-0.182	-0.224	.
phosphate	chem	.	.	0.019	-0.086	.	.
silicate	chem	-0.121	-0.003	-0.005	-0.040	-0.004	.

Table 6: Estimated β coefficients from the 10-cluster, 3-dimensional model in Section 3 (part 3 of 3). The column names Diam, Red and Orange refer to the names of the 3-dimensional cytogram axes.

Cluster 1		Cluster 2		Cluster 3	
Variable	Estim.	Variable	Estim.	Variable	Estim.
b2	0.077	phosphate	0.052	ftle_bw_sla	0.024
silicate	-0.016	p4	0.010	wind_stress	-0.029
ftle_bw_sla	0.005	p2	-0.004	p2	0.006
p4	-0.004	density	0.026	sla	0.001
pp	0.066	sdns	-0.002	b2	-0.023
sla	0.004	CHL	.	p3	0.005
p2	.	wind_stress	.	northward_wind	-0.008
ugos	0.005	Si	-0.021	eastward_wind	-0.020
par	0.002	p1	0.004	p1	0.000
nitrate	.	p3	.	b1	0.032
b1	0.014	vgos	.	ugosa	-0.005
o2sat	0.010	northward_wind	-0.009	p4	0.002
eastward_wind	-0.023	b2	-0.000	vgosa	.
p1	0.002	ugos	0.007	par	0.004
vgosa	.	silicate	-0.022	vgos	.
vgos	0.012	par	.	sdns	-0.010
northward_wind	.	sla	-0.012	density	.
CHL	-0.141	Fe	.	disp_bw_sla	0.004
AOU	.	nitrate	.	wind_speed	.
p3	0.007	sst	-0.028	phosphate	.
P04	0.024	pp	.	AOU	.
disp_bw_sla	0.001	vgosa	0.014	silicate	.
Si	0.014	ftle_bw_sla	.	o2sat	0.017
sdns	.	disp_bw_sla	.	sdns	.
wind_speed	.	ugosa	.	ugos	.
ugosa	.	wind_speed	.	sst	-0.004
density	.	eastward_wind	.	pp	-0.008
O2	0.071	o2sat	-0.004	sss	.
wind_stress	0.011	O2	.	P04	-0.001
sss	.	b1	.	Fe	-0.011
N03	.	AOU	.	CHL	.
sdns	.	P04	.	O2	.
oxygen	.	oxygen	.	nitrate	.
phosphate	.	salinity	.	Si	.
Fe	.	sss	.	N03	.
PHYC	.	N03	.	PHYC	.
salinity	.	PHYC	.	oxygen	.
sst	.	sdns	.	salinity	.
conductivity	.	conductivity	.	conductivity	.

Table 7: (Part 1 of 2) Stability of β coefficients (measured by how frequently nonzero it was estimated in subsamples) in clusters 1 through 3, shown along with original coefficient estimates in the full data. Within each column, variables are sorted by selection probability. Zeros are shown as '.', to distinguish with 0.000 or -0.000 which are small but nonzero numbers. As was mentioned in Table 1, the short hand of `sdns` and `sdes` is used for `surface_downward_northward_stress` and `surface_downward_northward_stress`, and the suffixes `_WDA_clim` are omitted.

Cluster 4 Variable	Cluster 4 Estim.	Cluster 4 P(nonzero)	Cluster 5 Variable	Cluster 5 Estim.	Cluster 5 P(nonzero)
sla	0.002	0.28	p2	0.013	0.96
wind_speed	0.033	0.25	sla	-0.022	0.93
p3	-0.003	0.23	p4	-0.006	0.91
p4	-0.002	0.23	p3	0.010	0.83
ftle_bw_sla	0.000	0.23	PP	.	0.78
wind_stress	.	0.22	ugos	0.058	0.74
silicate	-0.045	0.22	p1	0.008	0.70
b2	.	0.21	disp_bw_sla	-0.003	0.63
p1	-0.002	0.20	eastward_wind	0.021	0.47
p2	-0.006	0.20	par	0.002	0.33
par	-0.002	0.19	ftle_bw_sla	-0.011	0.32
vgos	.	0.18	b2	.	0.31
eastward_wind	.	0.18	ugosa	-0.050	0.31
vgosa	0.025	0.14	vgos	-0.006	0.30
disp_bw_sla	.	0.14	nitrate	.	0.30
sdns	.	0.11	sdns	.	0.27
ugosa	0.007	0.10	sss	-0.067	0.26
northward_wind	.	0.10	Fe	0.001	0.26
sss	.	0.08	vgosa	.	0.23
ugos	.	0.08	northward_wind	.	0.22
b1	0.038	0.07	PHYC	0.010	0.21
Si	.	0.07	wind_speed	.	0.19
AOU	.	0.07	silicate	-0.001	0.19
Fe	.	0.06	density	-0.038	0.18
sdns	-0.007	0.06	sst	-0.070	0.17
density	0.051	0.06	wind_stress	0.025	0.15
o2sat	.	0.06	sdns	0.011	0.15
phosphate	0.012	0.05	o2sat	-0.022	0.14
nitrate	.	0.04	phosphate	-0.132	0.12
sst	.	0.03	b1	0.046	0.11
PP	.	0.03	AOU	.	0.07
PHYC	.	0.03	CHL	.	0.05
PO4	.	0.03	Si	-0.006	0.04
CHL	.	0.01	oxygen	.	0.04
O2	.	0.01	PO4	.	0.03
salinity	.	0.01	O2	.	0.01
NO3	.	.	NO3	.	.
oxygen	.	.	salinity	.	.
conductivity	.	.	conductivity	.	.

Table 8: (Part 2 of 2) Continuing from table 7, we show the stability of β coefficients in clusters 4 through 5, along with original coefficient estimates in the full data.

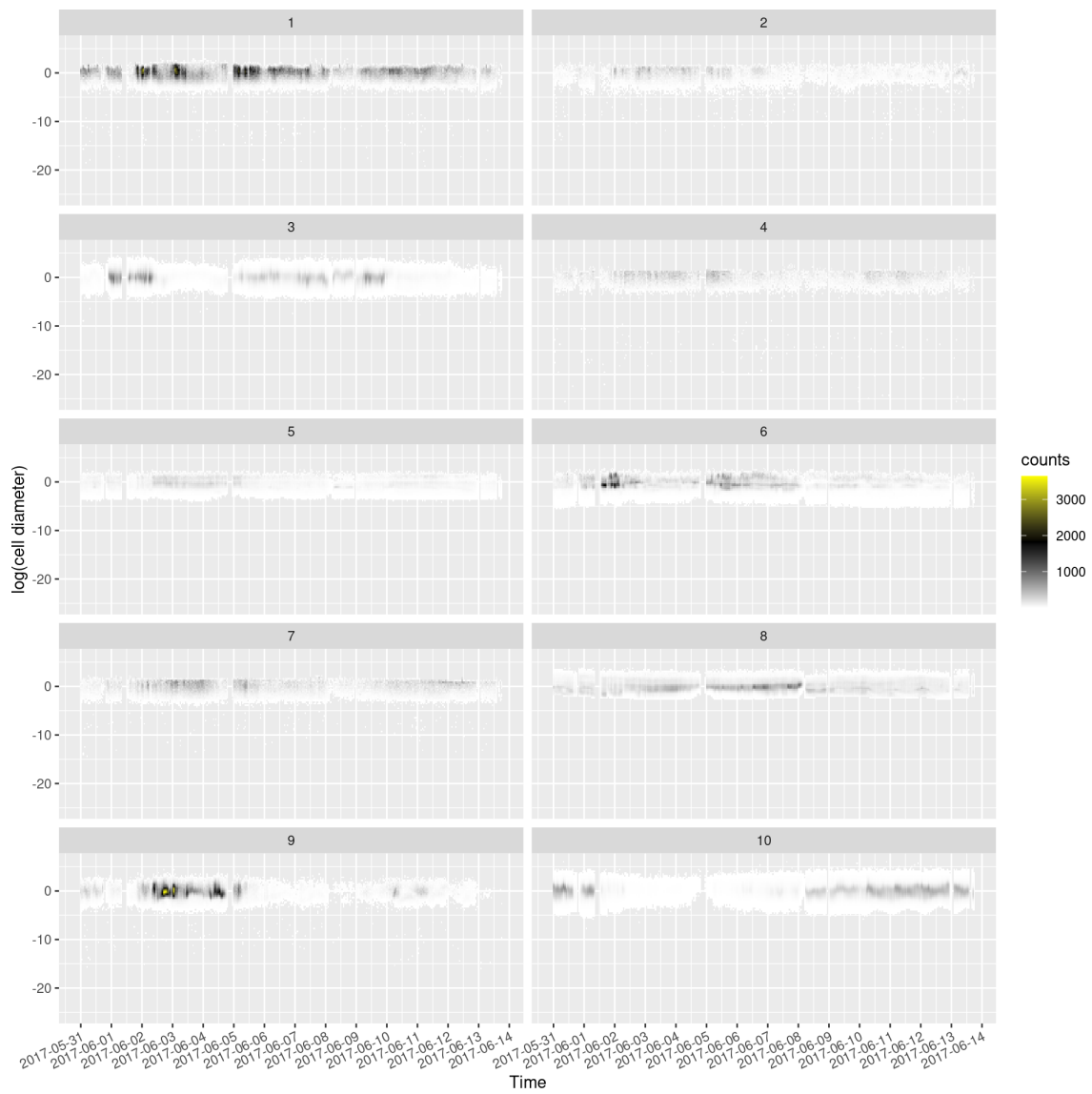


Figure 15: Each of the ten panels show the binned, 1-dimensional sphered residuals from a 10-cluster 3d model. The dimension (out of three) that is shown is the log cell diameter (called *Diam* elsewhere). For full details about the sphered residuals, see Supplement E.

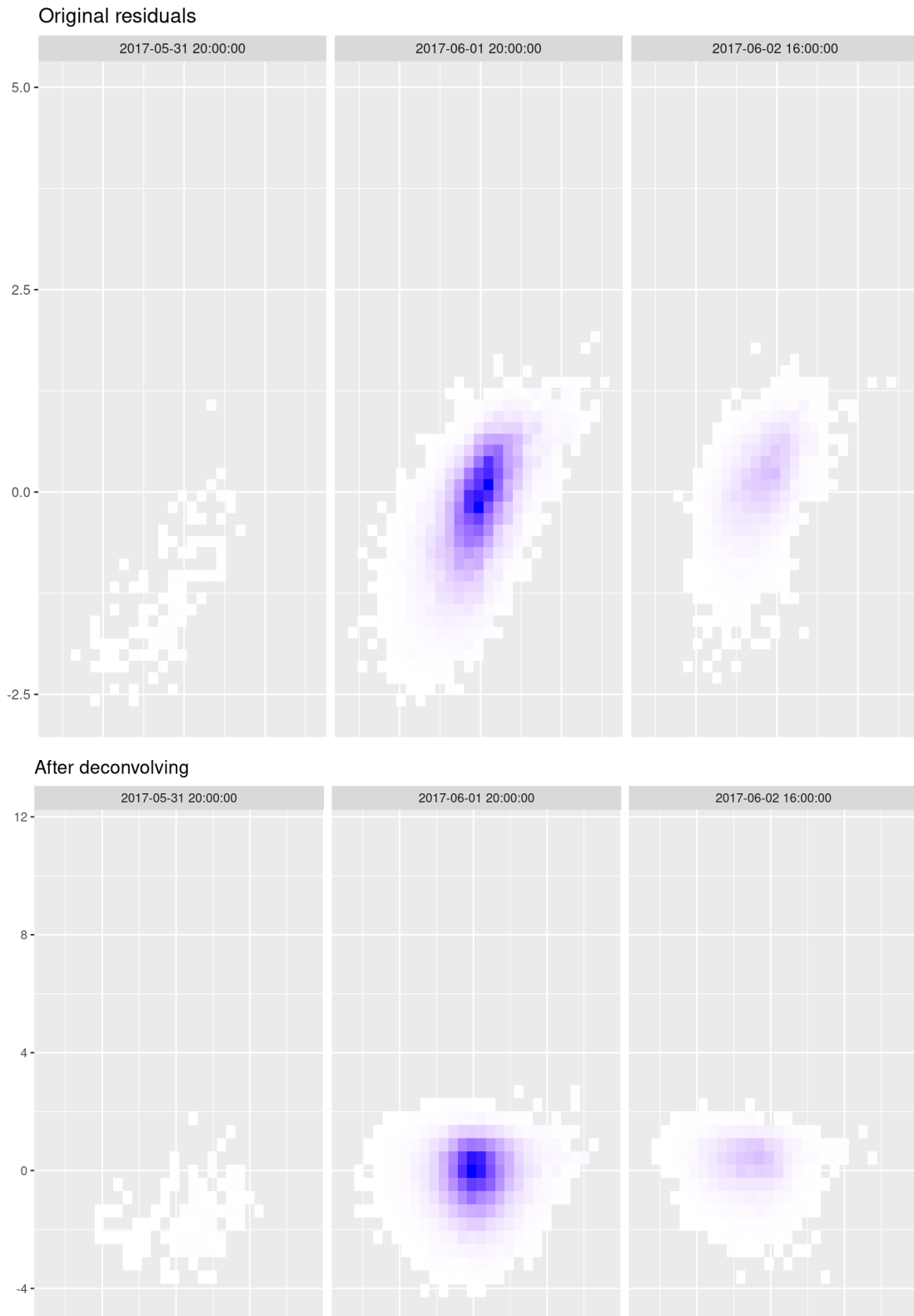


Figure 16: The top row shows, at three time points, two dimensions (*diam* and *chl*) of binned residuals from one cluster. The bottom row shows the sphered version of those same residuals. The sphering is done by left-multiplication of the square root $\mathcal{Q}\beta$ the estimated covariance matrix ($\Sigma_k^{-1/2}$) on the residuals. For full details, see Supplement E.

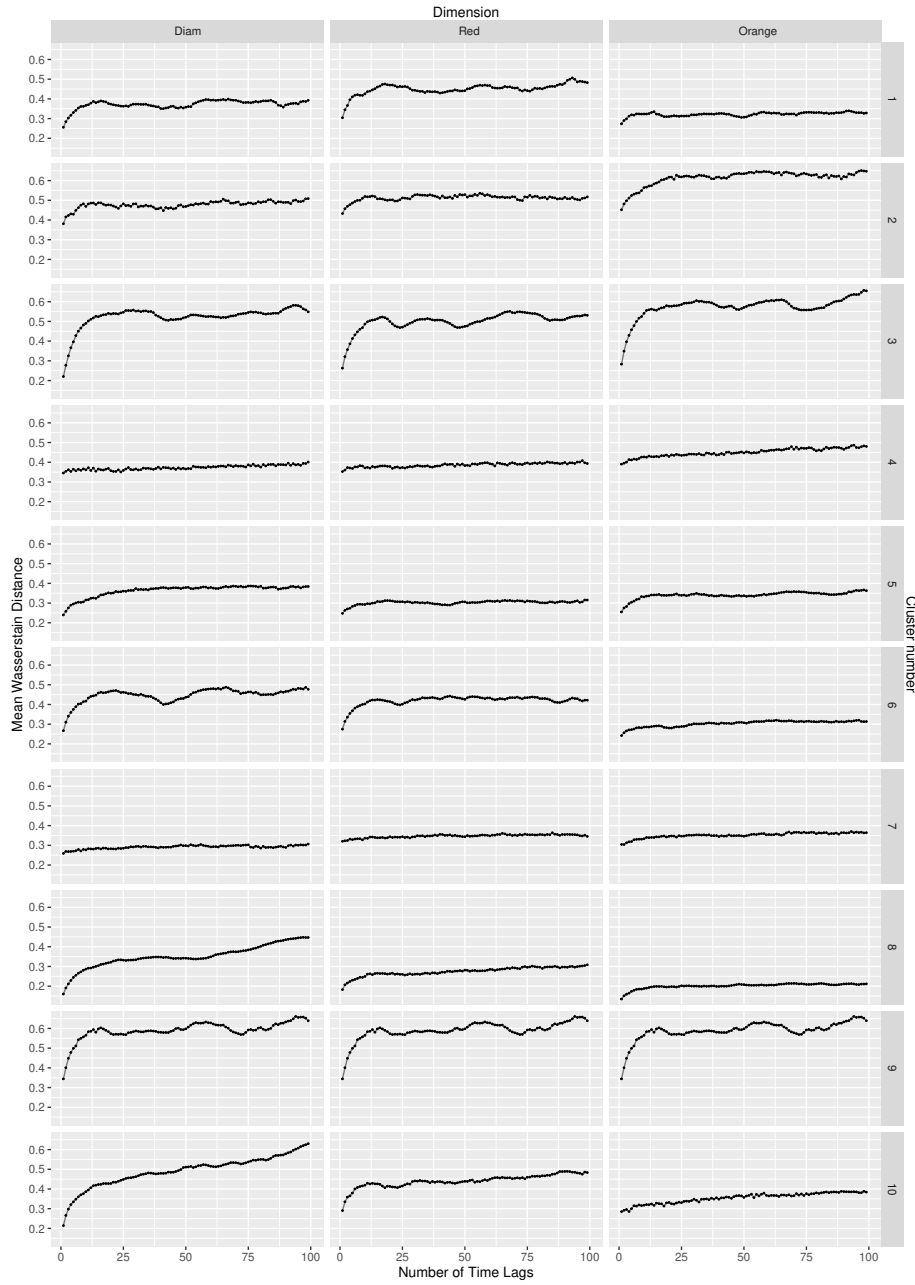


Figure 17: Each column is a dimension $m = 1, 2, 3$ corresponding to the cytogram axes *Diam*, *Red*, and *Orange*. Each row is a cluster k , ten in total. In each panel, the y-axis is the average l -lagged Wasserstein distance for cluster k in dimension m , $D_{m,k,l}$, as defined in (28) in Supplement E, and the x axis is lag l .

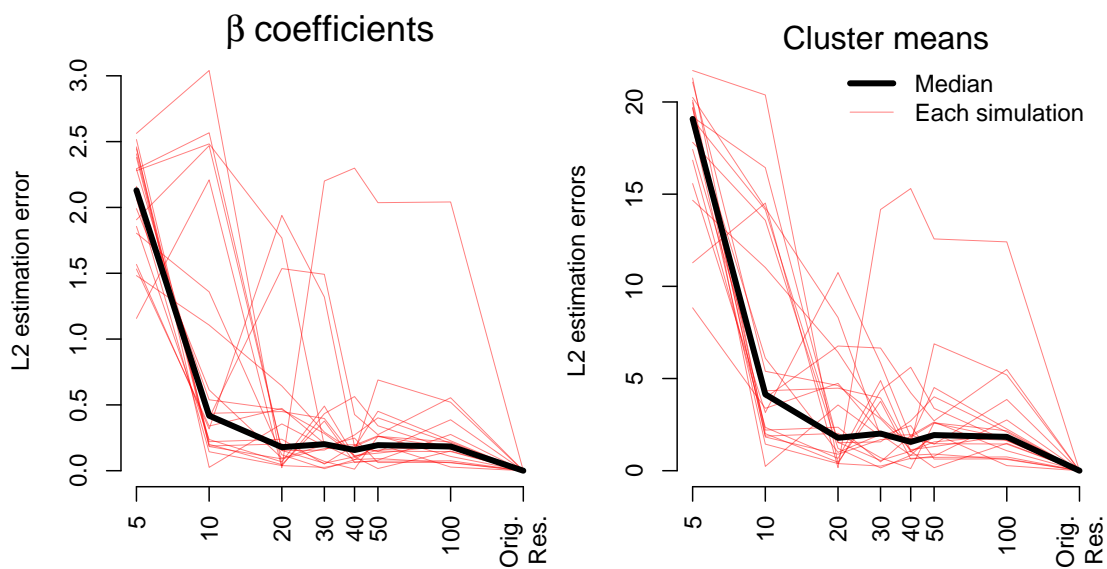


Figure 18: L2 estimation errors of the estimated models from binning, compared to the original data, over a varying number of bins (shown in the x axis). The left panel shows entry-wise L2 estimation error of the β coefficients, and the right panel shows that of the cluster means. (The right-most value is of every line of both plots equals zero, and the x axis is logarithmically spaced.) These plots show that the estimation error incurred by binning decreases rapidly, then plateaus at a low point for a relatively coarse bin resolution, of about $B = 20$.

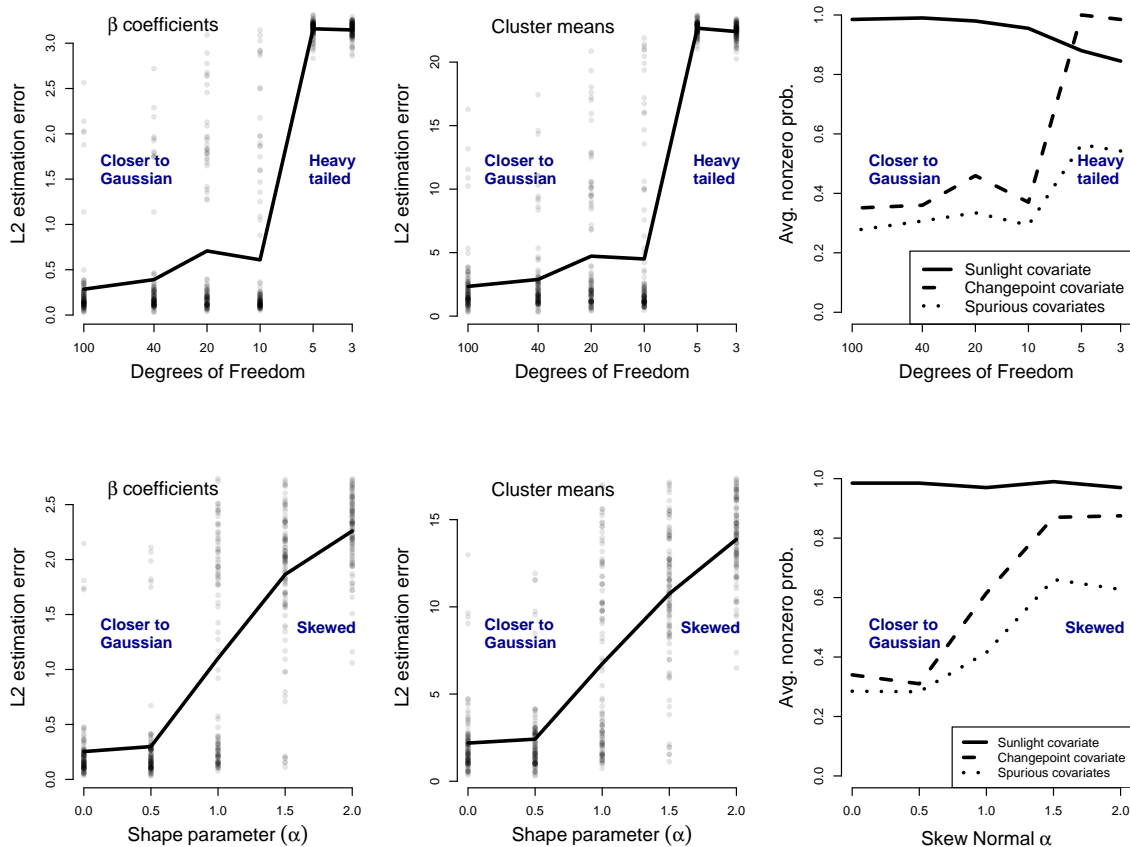


Figure 19: The top row shows the simulation results of the heavy-tail simulations, and the bottom row shows the results of the skewed-data simulations, described in Supplement F. In each row, three model performance metrics are shown – the left and middle panel show the entry-wise L2 estimation error of the β coefficients (left panel) and the cluster means (middle panel) with the average shown in the thick black line, and the right panel shows the variable selection performance. For each simulation setup (degrees of freedom or skewness parameter), 100 different datasets were generated and models were estimated on each dataset.